OPTIMISATION OF BIMETALLIC Co-NI SUPPORTED CATALYSTS FOR OXIDATION OF METHANE IN NATURAL GAS VEHICLES

A. Choya, B. de Rivas, J.R. González-Velasco, J.I. Gutiérrez-Ortiz, R. López-Fonseca

Applied Catalysis B: Environmental 284 (2021) 119712

DOI: 10.1016/j.apcatb.2020.119712

OPTIMISATION OF BIMETALLIC Co-Ni SUPPORTED CATALYSTS FOR OXIDATION OF METHANE IN NATURAL GAS VEHICLES

Andoni Choya, Beatriz de Rivas, Juan Ramón González-Velasco,

Jose Ignacio Gutiérrez-Ortiz, Rubén López-Fonseca*

Chemical Technologies for Environmental Sustainability Group,

Department of Chemical Engineering, Faculty of Science and Technology,

University of The Basque Country UPV/EHU, PO Box 644, E-48080 Bilbao, Spain

*Corresponding author:

Phone: +34-94-6015985

Fax: +34-94-6015963

E-mail address: ruben.lopez@ehu.eus

ABSTRACT

This work deals with the extensive study of supported bimetallic Co-Ni catalysts for the complete oxidation of methane. The simultaneous incorporation of nickel and cobalt was found to enhance the redox properties by favouring the formation of nickel cobaltite-like species and partially inhibiting the interaction between Co_3O_4 and alumina. In turn, this resulted in an increase of the amount of Co^{3+} cations in the catalysts, which led to a more notable presence of active lattice oxygen species in the samples. When the nickel loading was increased, the generation of less active NiO was observed. The improvement of the redox properties resulted in a promotion of the specific reaction rate and a shift of around 50 °C in the T_{50} value over the bimetallic catalysts. The most active catalyst (25Co-5Ni) was found to be relatively stable during prolonged operation times, but suffered an appreciable and irreversible deactivation in the presence of water vapour.

Keywords: methane oxidation; cobalt spinel; nickel cobaltite; lattice oxygen

1. Introduction

Nowadays the transport sector is one of the most important contributors to anthropogenic CO_2 emissions, mainly due to the extensive use of petroleum-derived fuels [1,2]. To solve this problem, it is clear that in the long-term future, transportation must chiefly rely on electricity and hydrogen fuel cells for its operation. However, these technologies are still under development and not currently ready for extensive use. Consequently, the use of alternative fuels with lower environmental impact, such as natural gas, can be an adequate and temporary solution since this type of fuel produces significantly lower CO_2 and NO_x emissions [3,4]. The use of vehicular natural gas, however, involves the essential need to efficiently control the emissions of unburned methane, as this greenhouse effect gas is on average 28 times more powerful than CO_2 [5,6].

Compared with adsorption, condensation, membrane separation or biofiltration, thermal and catalytic oxidation are more efficient for treating large gas flows with dilute methane (<1%vol). Thermal oxidation is a proven technology, already in use for removal of methane and VOCs in various applications such as biogas from landfills, ventilation air methane and coal mine methane or deodorisation in different industries. Thermal oxidation can treat streams with methane concentrations as low as 0.5%vol and can be coupled with an energy recovery system. Nevertheless, the temperature required to achieve complete thermal oxidation of methane is normally around 1,000 °C, which means that either compression or the addition of a secondary fuel are required to operate. Catalytic oxidation is essentially an upgrade of thermal oxidation. Since the use of the catalyst can take the reaction temperature down to the thermal level of the exhaust gases, this technique can be successfully implemented in vehicles and other mobile sources.

Traditionally, complete oxidation of methane over noble metals-based (Pd and Pt) catalysts has been the preferred option, but the scarcity and high price of these materials, along with their low thermal stability, are major barriers to their extensive application [7,8]. Co_3O_4-based catalysts, however, are much more available, and exhibit a notable activity for methane oxidation with an excellent selectivity to CO_2 over a wide operation temperature range. This class of catalyst is frequently supported over a porous media, such as gamma-alumina, to improve the typically poor structural and textural properties of this active phase [9,10]. Nevertheless, this implies a relevant shortcoming in the resulting catalyst since the strong cobalt-alumina interaction that frequently occurs is widely accepted to be detrimental to the redox properties of deposited Co_3O_4, which are essential for its oxidation ability. This interaction may provoke the conversion of Co_3O_4 into cobalt aluminate ($CoAl_2O_4$), an inactive species from where cobalt cannot be easily recovered into an active form [11,12].

Several approaches have been proposed to circumvent this obstacle. The first, and most obvious, would be to substitute the gamma-alumina with a different support. Nevertheless, of the materials available with a high specific surface, for instance silica, magnesia or zeolites, none of them exhibit a null interaction with cobalt. The performance of the resulting supported catalysts is negatively affected by the formation of inactive phases such as cobalt silicate, Co-Mg solid solutions or cobalt aluminate [13-15]. Some other studies have opted for supports showing a very low affinity for cobalt, namely alpha-alumina [16,17]. Unfortunately, the amount of active phase that can be deposited over this support is limited. Another alternative to overcome this problem would be to use a promoter to modify the gamma-alumina to tune its high affinity for deposited cobalt. This material is either introduced into the alumina lattice during its synthesis, with the aim of modifying its properties [18], or is deposited over

the surface of the already-formed alumina, prior to the deposition of cobalt, to serve as a physical barrier [19,20]. In any case, both approaches often result in a certain inhibition of cobalt aluminate formation. However, a side effect observed in most cases is the formation of stable mixed oxides between cobalt and the promoter, with a lower specific activity than Co_3O_4.

Taking all this background into consideration, it is reasonable to propose that a third, possible strategy could be the addition of a metallic promoter directly to the cobalt spinel phase. If cobalt and the selected promoter, intimately mixed, are deposited onto the alumina simultaneously, then the cobalt-promoter interaction should be, in principle, highly favoured, which would lead to a low formation of cobalt aluminate and an active cobalt phase with improved properties. To ensure this, the promoter should be chosen mainly on account of its ability to insert into the spinel lattice. For this reason, one of the most appropriate candidates could be nickel, due to its similar ionic radius, coordination and oxidation states with respect to cobalt.

Therefore, on the basis of the assumption that a cobalt-nickel catalyst will give synergetic catalytic properties, we tried to understand the chemical and structural characteristics of this type of bimetallic catalyst and to establish a relationship between the catalyst properties and its activity for lean methane oxidation. The investigated alumina-supported catalysts were prepared using co-precipitation and the total metallic loading of the investigated catalysts was fixed at 30%wt. [21]. Since the most active phase in these samples was expected to be predominantly cobalt oxide, the nickel loading was limited to a maximum of 15%wt. The ultimate objective is thus to identify the catalyst composition with a proper cobalt-nickel interaction that minimises the formation of cobalt aluminate and enhances the redox properties of the resulting active Co_3O_4 spinel phase.

2. Experimental

2.1. Synthesis of the bimetallic supported Co-Ni catalysts

The supported cobalt-nickel catalysts were prepared by a basic precipitation route with cobalt (II) nitrate hexahydrate ($Co(NO_3)_2 \cdot 6H_2O$, Fluka) and nickel (II) nitrate hexahydrate ($Ni(NO_3)_2 \cdot 6H_2O$, Merck) on a commercial γ-Al_2O_3 (Saint Gobain) thermally stabilised at 850 °C for 8 hours. For each support, 5 g of γ-Al_2O_3 were mixed with 100 mL of a solution with adjusted concentrations of Co and Ni nitrates. Then a solution of Na_2CO_3 1.2M was added dropwise until the pH reached 8.5. The temperature was kept constant at 80 °C. The selected cobalt loadings were 25, 20 and 15%wt., while the total metallic (Co+Ni) loading was 30%wt. for all samples. Accordingly, the nickel content of the samples was 5, 10 and 15%wt., respectively. After ageing the slurry for 30 minutes at constant temperature (80 °C) and pH (8.5), the obtained precipitates were filtered and washed with 5 litres of deionised hot water so as to remove traces of sodium ions from the catalyst surface [22]. The samples were denoted as xCo-(30-x)Ni where x stands for the nominal cobalt loading. Monometallic cobalt and nickel catalysts supported on alumina with a 30%wt. loading along with bulk NiO, Co_3O_4 and $NiCo_2O_4$ were also synthesised by the same route.

All precursors were dried at 110 °C for 16 hours and then calcined at 600 °C in static air to produce the oxide catalysts. As derived by the thermogravimetric analysis of the oxidative decomposition of a cobalt catalytic precursor (see Figure S1, Supplementary material), this thermal treatment involved three consecutive steps at 125 ºC (5 °C min^{-1}), 300 ºC (1 °C min^{-1}) and 600 ºC (5 °C min^{-1}). Finally, the samples were kept at this temperature for 4 hours [21].

2.2. Characterisation techniques

Wavelength Dispersive X-Ray Fluorescence (WDXRF) was employed to determine the composition of the synthesised catalysts. A boron pearl glass was prepared with a commercial flux agent (Spectromelt A12). Thus, a mixture with a catalyst:flux agent mass ratio of 1:20 was melted at 1200 °C. The analysis was performed under vacuum with a Malvern Panalytical AXIOS WDXRF spectrometer coupled with a Rh tube and three different detectors (gas flow, scintillation and Xe sealed). The surface area, pore volume and pore size distribution were evaluated by low-temperature N_2 physisorption with a Micromeritics TriStar II instrument following the BET and BJH methods. Prior to adsorption at -196 ºC, the samples were subjected to degassing with flowing N_2 in a Micromeritics SmartPrep unit at 300 °C for 10 hours.

X-ray diffraction (XRD) data were collected on a X'PERT-PRO X-Ray diffractometer using Cu Kα radiation (λ = 1.5406 Å) and a Ni filter at 40 kV and 40 mA. The patterns were recorded with a step size of 0.026° and a counting time of 2.0 seconds. The cell parameter of the Co-spinel phase was estimated by profile matching (FullProf.2k software) of the pattern. The experimental diffraction patterns were compared with ICDD (International Centre for Diffraction Data) database cards. Raman spectra in the 150-1200 cm^{-1} range were obtained with a Renishaw InVia Raman spectrometer operating with a 514 nm laser source (ion-argon laser, Modu-Laser). The samples were additionally characterised by X-Ray photoelectron spectroscopy (XPS). Spectra were collected with a Kratos AXIS Supra spectrometer (225 W Al Kα radiation source) with a pass energy of 20 eV.

Scanning Transmission Electron Microscopy - High Angle Annular Dark Field (STEM-HAADF) and High Resolution Transmission Electron Microscopy (HRTEM) images were obtained in a CETCOR Cs-probe-corrected Titan microscope (ThermoFisher

Scientific, formerly FEI) at a working voltage of 300 kV, coupled with a HAADF detector (Fischione). The instrument had a normal field emission gun (Shottky emitter) equipped with a SuperTwin lens and a CCD camera. The samples were sonicated in ethanol and dropped onto a holey amorphous carbon film supported on a copper grid. The TEM apparatus was also equipped for X-ray Energy Dispersive Spectroscopy (EDS) and Electron Energy Loss Spectroscopy (EELS) experiments. Both spectroscopic techniques, when combined with the imaging technique, were able to provide spatially resolved elemental analysis of the samples. EDS spectra were obtained with an EDAX detector. For EELS analysis the microscope was fitted with the Tridiem Gatan Energy Filter. A 2k x 2k Ultrascan CCD camera (Gatan) was positioned before the filter for TEM imaging (energy resolution of 0.7 eV). The acquisition time for the analysis was 50 ms per spectrum and the used energy dispersion was 0.2 eV $pixel^{-1}$.

The redox behaviour of the cobalt catalysts was examined by temperature-programmed reduction with hydrogen (H_2-TPR) with a Micromeritics Autochem 2920 equipment with a 5%H_2/Ar stream. Previously, the samples were treated at 300 °C for 30 minutes with a flowing 5%O_2/He mixture, after which they were cooled down to 50 °C under inert conditions. The reduction process was conducted up to 950 °C at a heating rate of 10 °C min^{-1} with a simultaneous removal of formed water. The samples were kept at this temperature for 10 minutes. Likewise, the mobility of oxygen species and their ability for the activation of methane was examined by temperature-programmed reaction (CH_4-TPRe) with a 5%CH_4/He mixture. The exit stream was continuously analysed by mass spectrometry (MKS Cirrus Quadrupole Mass Spectrometer). The runs were conducted between 50-600 °C (10 °C min^{-1}) with a subsequent isothermal step for 30 minutes.

2.3. Catalytic activity determination

The catalytic performance was examined in a Hastelloy X fixed bed reactor (Microactivity by PID Eng&Tech S.L.). A K type thermocouple was placed in the middle of the catalyst bed for controlling the reaction temperature. The bed was a mixture of 1 g of catalyst (sieve fraction of 0.25-0.3 mm) diluted with 1 g of inert quartz (sieve fraction of 0.5-0.8 mm). A gaseous stream with a total flow of (500 mL min^{-1}) and containing CH_4 (1%), O_2 (10%) and N_2 (89%) was fed at a weight hourly space velocity of 300 mL CH_4 g^{-1} h^{-1} under atmospheric pressure (30,000 h^{-1}).

Catalytic conversion was examined between 200-600 °C in steps of 25 °C. The reaction products were quantified with an on-line gas chromatograph (Agilent Technologies 7890N) equipped with a thermal conductivity detector. Further details on the analysis of the exit stream are given elsewhere [21]. The absence of heat or mass transfer limitations affecting the kinetic results was verified according to the criteria dictated by Eurokin [23,24] (Table S1, Supplementary material). Additionally, the stability of the most active sample with time on stream was studied at constant temperature (550 °C) for a total reaction interval of 150 hours while under cycling dry/humid (10%vol. H_2O) conditions every 25 hours.

3. Results and discussion

3.1. Characterisation of the Co-Ni catalysts

The elemental composition of the nickel-cobalt catalysts was determined by WDXRF. Chemical analysis revealed that the amount of each deposited metal (cobalt and nickel) on the alumina support was relatively similar to the respective nominal loading (Table 1). The textural and structural properties of the nickel-cobalt catalysts were investigated by N_2-physisorption, XRD, Raman spectroscopy, XPS, STEM-HAADF

coupled to EELS and EDX and HRTEM. The blank gamma alumina support showed a surface area of 139 $m^2 g^{-1}$ and a pore volume of 0.56 $cm^3 g^{-1}$ (Table 1). The coprecipitated samples revealed a slightly lower surface, in the 113-123 $m^2 g^{-1}$ range, with a concomitant decrease in pore volume of around 30-40%. The samples revealed type IV isotherms with H2 hysteresis loops, typically assigned to pore blocking in materials with a wide pore size distribution (Figure S2, Supplementary material). After metallic deposition no major alteration of the hysteresis loops was observed. According to the BJH method the bare alumina support was characterised by a bimodal pore size distribution centred at 90 and 150 Å that became a unimodal distribution peaking at about 90 Å for the Co-Ni catalysts, probably due to the narrowing of the largest pores (150 Å) caused by the addition of the active phases irrespective of their relative proportion. In relation to the pore volume, the lowest value (0.29 $cm^3 g^{-1}$) was measured over the 30Co sample. When Ni was present, this appreciably increased up to 0.35-0.40 $cm^3 g^{-1}$. These larger values were assigned to the presence of a significant fraction of large pores of around 125 and 340 Å, mainly over the Ni-rich 15Co-15Ni catalyst. As will be shown later, this increase in the pore volume could be taken as preliminary evidence of the formation of a $NiCo_2O_4$-like phase in the bimetallic catalysts. Note that this bulk oxide was characterised by wide pores with a size of around 320 Å (Table 1).

TABLE 1

It is commonly accepted that the characterisation by XRD of gamma-alumina supported Co,Ni-containing catalysts is often not useful for obtaining a clear picture of the nature of the eventually present phases since Co_3O_4 (ICDD 00-042-1467), $CoAl_2O_4$ (ICDD 00-044-0160), $NiAl_2O_4$ (ICDD 00-078-1601) and $NiCo_2O_4$ (ICDD 00-002-1074) spinel oxides possess a virtually identical cubic (Fd-3m) crystalline structure. Note that the existence of appreciable amounts of both amorphous cobalt aluminate and nickel

aluminate was plausible owing to the interaction of Co_3O_4 and NiO with γ-Al_2O_3 at mild temperatures (600 °C) [25,26]. Therefore, the patterns of the Co-Ni catalysts, shown in Figure S3, Supplementary material, evidenced several signals at 2θ = 31.3, 37.0, 45.1, 59.4 and 65.3°, which were consistent with the presence of one or several crystalline spinelic phases. In addition, the bimetallic catalysts with a higher Ni loading (20Co-10Ni and 15Co-15Ni) along with the 30Ni sample revealed signals located at 2θ = 43.9 and 62.9º attributable to the presence of segregated NiO (ICDD 00-089-7131) crystallites with sizes of around 14-19 nm. The crystallite size of this oxide phase was estimated from the Full Width Half Maximum (FWHM) of the characteristic peak located at 43.9°, which corresponded to the (200) plane, by applying the Scherrer equation. As for the 30Ni sample, it should be remarked that, although the presence of nickel aluminate was highly probable, its diffraction pattern did not reveal individual signals assignable to this crystalline spinel phase. As aforementioned, an unambiguous identification of the cobalt species (Co_3O_4 and/or $CoAl_2O_4$) present in the 30Co sample was not possible. However, since it is known that the $CoAl_2O_4$ phase formed below 600 °C possesses a notable amorphous character [27,28], its signals are usually assumed to be weaker compared with those of more crystalline Co_3O_4. Therefore, although the simultaneous presence of various spinels in the coprecipitated samples could not be initially discerned owing to their similar diffraction patterns, it could be reasonably expected that the observed high-intensity spinel signals should be preferentially attributed to either Co_3O_4 or $NiCo_2O_4$ phases. In fact, an enlarged view of the main spinel signal at 2θ = 37.1° of the bimetallic catalysts (Figure 1) revealed a continuous shift towards a lower angle value with increasing Ni loading. Thus, the signal of the 15Co-15Ni sample (2θ = 37.0°) was relatively close to that of the bulk $NiCo_2O_4$ sample (2θ = 36.7°), thereby suggesting the favoured presence of this spinel over the Co-Ni

catalysts. The structural change of the Co-spinel lattice was further established by comparing the cell size of the 30Co catalyst, the bimetallic counterparts, and the as-synthesised bulk nickel cobaltite. Results included in Table 1 indicated a gradual enlargement of the cell parameter when nickel was present, from to 8.096 Å over the 30Co catalyst to 8.109 Å over the 15Co-15Ni catalyst. The growing trend towards the limit value of bulk nickel cobaltite (8.123 Å) pointed to the formation of this new oxide phase over the bimetallic samples. On the other hand, the introduction of nickel also led to a decrease in the crystallite size (Table 1) of the spinel-like phase, from 29 nm for the 30Co catalyst to 21-23 nm for the Co-Ni coprecipitated samples. The mean crystallite size of this phase was calculated from the peak broadening (FWHM) of the most intense reflection ((311) plane, 2θ at 37.1º) using the Scherrer equation as well.

FIGURE 1

The structure of the samples was also examined by Raman spectroscopy. The Raman spectra (Figure 2) of the 30Co sample displayed the typical five vibration modes of Co_3O_4 at 196, 520 and 619 cm^{-1} (F_{2g}), 480 cm^{-1} (E_g) and 687 cm^{-1} (A_{1g}) [29]. Additionally, two shoulders at 705 and 725 cm^{-1} related to the $CoAl_2O_4$ spinel were observed [30,31]. On the other hand, the spectrum of the 30Ni sample suggested the presence of both NiO and $NiAl_2O_4$ phases, in spite of the fact that the latter was not directly observed by XRD probably due to its amorphous character. Hence, the main signal for this sample was located at 545 cm^{-1}. This Raman mode was between the main signals of NiO (510 cm^{-1}) and $NiAl_2O_4$ (574 cm^{-1}) [32,33], which evidenced a significant presence of both nickel phases. As suggested later on by H_2-TPR analysis, their relative abundance accounted for about 30%(NiO)/70%($NiAl_2O_4$). Also, the second order phonon of NiO at 1080 cm^{-1} (not shown) and weaker signals from nickel aluminate at 250, 746 and 835 cm^{-1} were observed [34].

FIGURE 2

As for the bimetallic catalysts, these only showed four (196, 480, 520 and 687 cm^{-1}) out of the five signals assigned to the Co_3O_4 spinel. The signal at 619 cm^{-1} was not visible due to the appearance of a wide vibration band in the 540-650 cm^{-1} range, similar to that displayed by the as-prepared bulk $NiCo_2O_4$. Furthermore, these Raman modes significantly shifted towards lower values, especially for the 25Co-5Ni and 20Co-10Ni samples. This accordingly indicated some degree of distortion of the spinel Co_3O_4 lattice owing to the partial insertion of Ni^{2+} cations [35], as also revealed by XRD. On the other hand, the aforementioned shoulders of cobalt aluminate were less evident.

The surface chemical state of the bi- and monometallic catalysts was investigated by XPS. For the sake of comparison, the bulk $NiCo_2O_4$ sample was also examined. The surface composition and the distribution of nickel, cobalt and oxygen species was determined by deconvolution and integration of the $Ni2p_{3/2}$ (850-870 eV), $Co2p_{3/2}$ (777-792 eV) and O1s (526-536 eV) spectra, respectively, as shown in Figure 3. Firstly, the $Co2p_{3/2}$ spectra were deconvoluted into three main and two satellite contributions. The first two main components, centred at 779.5 and 780.7 eV, were attributed to the existence of Co^{3+} and Co^{2+} ions, respectively, while the third one, centred at 782.4 eV, was assigned to the presence of Co^{2+} as CoO [36]. Generally, its contribution was lower than 10% of the total surface Co concentration. This oxide was formed due to partial reduction of surface Co_3O_4 species as an unavoidable consequence of being exposed to the vacuum conditions in the XPS spectrometer. Therefore, it can be assumed that this phase was not present in the catalyst formulation. The signals located at 785.5 and 789.5 eV were identified as the shake-up satellite peaks of the Co^{2+} and Co^{3+} ions, respectively [37]. Likewise, the $Ni2p_{3/2}$ was deconvoluted following a similar procedure. Hence, three main peaks located at 853.9, 855.4 and 856.9 eV were noted,

which were related to the presence of Ni^{2+} as NiO species, the existence of Ni^{2+} belonging to a spinel lattice and the formation of Ni^{3+} species, respectively [38,39]. The satellite peak of the nickel spectra was dominated by an intense signal centred at 861.0 eV, characteristic of the marked presence of nickel in the +2 oxidation state, with a small shoulder located at around 865.3 eV assignable to a relatively small amount of Ni^{3+} species in the samples. Finally, the O1s spectra were deconvoluted into three components at 529.3, 531.3 and 532.6 eV. The first two peaks were attributed to lattice and adsorbed oxygen species, respectively, while the last one was assigned to the oxygen from various oxygen-containing groups including carbonates, water and hydroxyl species [40,41]. The surface composition estimated from these spectra is included in Table 2, along with the bulk composition determined by WDXRF for the sake of comparison. As expected, the aluminium concentration on the surface was appreciably lower. On the other hand, no marked differences in Co concentration were observed between the surface and the bulk. By contrast, a favoured accumulation of nickel at the surface level was evident for all the samples, with remarkably higher Ni concentrations (almost twice as much) when compared with the loading determined by WDXRF.

FIGURE 3

TABLE 2

The main band of the $Co2p_{3/2}$ spectra of the 30Co catalyst was located at 781.2 eV. This position was influenced by the notable presence of Co^{2+} species as $CoAl_2O_4$, in line with the results from Raman spectroscopy. In fact, the Co^{3+}/Co^{2+} molar ratio was as low as 0.67. With the addition of small amounts of nickel (5%wt.) the binding energy of this band significantly decreased to 779.8 eV. This shift was connected with a lower abundance of Co^{2+} species as cobalt aluminate. As shown in Figure 4, a further increase

in Ni loading did not lead to remarkable changes in the position of the band (779.9 eV for both 20Co-10Ni and 15Co-15Ni samples). More importantly, irrespective of the Ni content of the catalyst, the position was close to that observed for both bulk Co_3O_4 and $NiCo_2O_4$ (779.5 eV). Note that these two oxides were characterised by quite high Co^{3+}/Co^{2+} molar ratios (1.96 and 2.10, respectively). In view of the results included in Table 2 the presence of Co^{3+} species was most favoured for the lowest Ni content (25Ni-5Co sample, with a Co^{3+}/Co^{2+} molar ratio of 1.21). However, the origin of this considerable relative increase in the presence of Co^{3+} species as Co_3O_4 or $NiCo_2O_4$ cannot be clearly assessed.

To obtain an insight into this question, the $Ni2p_{3/2}$ spectra were analysed in detail. As stated earlier, the predominant nickel phases were Ni^{2+} as NiO or in the form of either $NiAl_2O_4$ or $NiCo_2O_4$. As reflected in Table 2, the presence of NiO was favoured by high Ni loadings with the Ni^{2+}(NiO)/Ni^{2+}(spinel) molar ratio increasing from 0.21 over the 25Co-5Ni sample to 0.89 over the 15Co-15Ni sample. On the other hand, while no remarkable changes were observed in the position of the Ni^{2+}(NiO) band, some significant alterations were evident for the band associated with Ni^{2+} species belonging to a spinelic lattice (Figure 4). It is noteworthy that this band was located at 855.7 eV for the 30Ni catalyst, which only contained $NiAl_2O_4$ along with NiO. Conversely, this band was positioned at 855.1 eV for the bulk $NiCo_2O_4$ sample. Therefore, the relative position with respect to these two reference values may be helpful in at least qualitatively defining the nature of the spinel that was preferably formed on the catalysts as a function of its nickel content. The trend visualised in Figure 4 pointed to a preferred formation of nickel cobaltite over the catalysts with small amounts of nickel while the Ni-rich samples were more prone to the generation of nickel aluminate. These findings thus confirmed that the high Co^{3+}/Co^{2+} molar ratio of the 25Co-5Ni sample

was due to the formation of $NiCo_2O_4$ at the expense of Co_3O_4. Finally, data collected in Table 2 revealed that this increase in the amount of Co^{3+} species was in turn accompanied by a marked presence of lattice oxygen species. These have been considered as the active species for methane oxidation according to a Mars-van Krevelen mechanism. As shown in Figure 5, the presence of this type of species was optimised for the 25Co-5Ni catalyst. Also note that, regardless of the Ni content, lattice oxygen species were more abundant, with O_{ads}/O_{latt} molar ratios in the 0.94-1.10 range, than in the monometallic counterparts (1.41 and 1.54 for the 30Co and 30Ni samples, respectively).

FIGURE 4

FIGURE 5

All the examined catalysts including the supported mono- and bimetallic catalysts and the bulk $NiCo_2O_4$ and NiO oxides contained a significant fraction of Ni^{3+} species. The corresponding Ni^{3+}/Ni^{2+} molar ratios are included in Table 2. The assessment of the origin of this signal is complex since Ni^{3+} may be related to the mixed Co-Ni spinel [42] but also to Ni_2O_3 derived from the surface oxidation of NiO [43,44]. It was found that Ni^{3+} species are more abundant with the Ni loading of the supported catalysts, from 0.13 over the 25Co-5Ni sample to 0.30 over the 30Ni sample. This trend was consistent with the increasing NiO content of the catalysts, as dictated by XRD and Raman spectroscopy. Note that the as-synthesised bulk NiO sample exhibited a molar ratio as high as 0.50. On the other hand, the presence of Ni^{3+} species in the 25Co-5Ni sample could be attributed to nickel cobaltite in view of its reduced amount of NiO.

An attempt to gain a more defined view of the surface chemical structure of the cobalt-nickel catalysts was made by studying their elemental composition. The bimetallic catalysts along with the monometallic 30Co and 30 Ni samples were thus characterised

by scanning transmission electron microscopy–high-angle annular dark field (STEM–HAADF). Moreover, EELS elemental maps (Figure 6) were obtained for certain regions in each sample to examine the spatial distribution of both metals in the Co-Ni catalysts. The 30Co and 30Ni catalysts were characterised by the presence of Co_3O_4 and NiO polycrystallites with sizes ranging from 20-40 and 10-30 nm, respectively (in some cases formed by the apparent attachment of smaller crystallites). On both samples, the abundance of relatively large regions of less crystalline aluminates was evidenced as well. With respect to bimetallic Co-Ni catalysts, nickel was homogeneously present and well mixed with cobalt when the Ni content was low (5%wt.%), thus expectedly favouring the formation of $NiCo_2O_4$-like species. Small Ni-containing patches assigned to isolated NiO with a size of 10-20 nm were observed as well. For increased Ni loadings in the catalyst (20Co-10Ni and 15Co-15Ni samples), noticeably larger areas (>50 nm) of Ni-rich phases (NiO and $NiAl_2O_4$) were observed.

FIGURE 6

Complementary EDX analysis was useful for giving information on the elemental concentration of selected spots of each sample (ESVision/TIA software). About 17 spot EDX analyses of each sample were performed, except for the 30Ni sample (4 spot measurements). These data provided a semi-quantitative distribution of the various species that were present on the samples as a function of the catalyst formulation. These included alumina, Co_3O_4, NiO, Ni-Al, Co-Al, Ni-Co and Ni-Co-Al species. This assignment was tentatively carried out as function of the relative abundance of Co, Ni, Al and O elements. Results corresponding to the oxide phase distribution over the monometallic and bimetallic catalysts are included in Figure 7. Figure S4, Supplementary material includes representative images of the microstructure of the investigated catalysts, with the EDX spectra of some selected analysed spots. In line

407 with the EELS maps, the 30Co catalyst consisted of a mixture of Co_3O_4 polycrystallites
408 and Co-Al entities attributable to cobalt aluminate-like species. In addition, some areas
409 of uncovered alumina support could be identified. Analogously, the pure nickel sample
410 (30Ni) presented relatively well-defined NiO crystallites and regions with nickel and
411 aluminium intimately in contact forming amorphous $NiAl_2O_4$-like species.

412 FIGURE 7

413 The analysis of the three bimetallic catalysts evidenced the presence of species with a
414 greater compositional variety including up to seven different oxide phases. Moreover,
415 remarkable changes in the relative abundance as a function of their composition were
416 observed. Hence, the cobalt present in the 25Co-5Ni catalyst was mainly in the form of
417 Ni-Co(40%), Co_3O_4(20%), Co-Al(20%), and Ni-Co-Al(13%) entities. The Ni-Co
418 species, which showed a Ni/Co molar ratio ranging between 0.1 and 0.2, were ascribed
419 to substoichiometric nickel cobaltite. As the cobalt loading decreased, the relative
420 amounts of Co_3O_4 species also decreased to 17% and 6% over the 20Co-10Ni and
421 15Co-15Ni samples. Likewise, Ni-Co species gradually tended to be less abundant,
422 particularly over the 15Co-15Ni catalyst (22%). Simultaneously, Ni-rich entities such as
423 NiO (with a Ni/Co molar ratio higher than 3) and Ni-Co-Al were favoured with higher
424 Ni content in the sample, up to 22% and 33%, respectively. It is worth pointing out that
425 results from EDX analysis were in agreement with the conclusions derived from the
426 spectroscopic techniques (Raman spectroscopy and XPS) and XRD, which suggested
427 the favoured formation of $NiCo_2O_4$-like species over the 25Co-5Ni catalyst, and the
428 generation of increasing amounts NiO over the 20Co-10Ni and 15Co-15Ni samples.
429 The samples were also examined by HRTEM. Figure S5, Supplementary material
430 shows selected HRTEM images for the 30Co and the three bimetallic catalysts. Over
431 the four samples the characteristic lattice fringes with interplanar spacing of 0.244 and

0.286 nm assignable to the {311} and the {220} planes of a spinel crystalline phase could be observed. As stated earlier, since the crystallographic parameters of Co_3O_4, $CoAl_2O_4$ and $NiCo_2O_4$ are virtually identical, it is rather difficult to distinguish them by electronic microscopy. Conversely, the TEM images of the 30Ni sample did not reveal the existence of the crystalline $NiAl_2O_4$ spinel. On the other hand, when analysing the results corresponding to the 20Co-10Ni and 15Co-15Ni samples (Figure S6, Supplementary material) individual crystallites presenting interlayer distances of 0.209 nm attributable to the spacing of the {200} plane of NiO were also clearly observed. Thus, the presence of segregated nickel oxide along with crystalline spinelic phases was corroborated over the Ni-rich bimetallic catalysts, in line with XRD, XPS and chemical mapping analysis.

The analysis of the samples by H_2-TPR was adequate not only for determining their redox behaviour but also in further corroborating the nature of the oxides phases present in the bimetallic catalysts, as tentatively established by XRD, Raman spectroscopy, XPS and STEM-HAADF and HRTEM. The corresponding profiles, including that of bulk nickel cobaltite, are included in Figure 8. Firstly, the reducibility of the supported monometallic oxides, namely 30Ni and 30Co catalysts, was discussed. As a reference, the redox properties of the bulk pure oxides (NiO and Co_3O_4) were also examined (Figure S7, Supplementary material). Briefly, bulk nickel oxide showed a broad profile with a peak reduction temperature at around 420 °C with a shoulder at 525 °C, which was coherent with the redox behaviour of NiO crystallites with a relatively large size (>40 nm, as determined by XRD). The profile of bulk Co_3O_4 was in concordance with a two-step $Co^{3+} \rightarrow Co^{2+} \rightarrow Co^0$ reduction process peaking at 310 and 380 °C, respectively. The shape of the reduction trace of bulk $NiCo_2O_4$ was similar to that of Co_3O_4 although the former seemed to be more easily reduced. Thus, its H_2 consumption started at

457 significantly lower temperatures, around 180 °C (about 210 °C for Co_3O_4). The
458 reduction process consisted of the reduction of Co^{3+} to Co^{2+} (260 °C) followed by the
459 simultaneous reduction of Co^{2+} and Ni^{2+} (at 340 °C) to the respective metallic states.
460 The 30Ni sample revealed an H_2 uptake at 425 ºC that was assigned to the reduction of
461 nickel oxide, in agreement with the profile of the bulk NiO [45]. A second noticeable
462 consumption was seen at 700 ºC, thereby revealing that this catalyst contained a
463 significant amount of hardly reducible $NiAl_2O_4$ species [46]. The overall H_2 uptake of
464 the sample was 4.5 mmol H_2 g^{-1}, very close to the theoretical value (4.6 mmol H_2 g^{-1}).
465 Note that the H_2:Ni reduction stoichiometry was 1:1 for both NiO and $NiAl_2O_4$. As for
466 the 30Co sample two reduction features were also observed. A first reduction event took
467 place at relatively low temperatures (in the 200-450 ºC range) that corresponded to the
468 aforementioned two-step reduction of Co_3O_4 to metallic cobalt, with two intermediate
469 temperature peaks at about 310 and 380 ºC [47,48]. At higher temperatures an
470 appreciable uptake at 660 ºC was also evident, which was related to the reduction of
471 $CoAl_2O_4$ [49,50]. Accordingly, the total H_2 consumption (5.2 mmol H_2 g^{-1}) was lower
472 than that expected for the exclusive presence of Co_3O_4 in the sample (6.8 mmol H_2 g^{-1}).
473 Recall that the H_2:Co reduction stoichiometry is 4:3 for Co_3O_4 and 1:1 for $CoAl_2O_4$.
474 Therefore, the high affinity of both nickel and cobalt for alumina unavoidably induced
475 the formation of highly stable aluminate species, as evidenced by XPS, Raman
476 spectroscopy and STEM-HAADF coupled to EDX that ultimately negatively influenced
477 the amount of low-temperature active oxygen species.
478 FIGURE 8
479 The H_2-TPR profiles of the alumina supported Co-Ni samples are included in Figure 8.
480 Similarly to the 30Co sample, the bimetallic catalysts exhibited two reduction processes
481 at distinctly different temperature windows located at 175-500 ºC and 500-900 ºC. The

H_2 consumption detected at the high temperature range revealed that the samples still possessed a significant fraction of metallic oxides in the form of aluminates with a high resistance to reduction. Another relevant finding was that the reduction process was significantly accelerated with the presence of relatively low amounts of nickel, namely 5 and 10%wt. Thus, it started at about 175 ºC over the 25Co-5Ni sample and 200 ºC over the 20Co-10Ni catalyst. However, no marked differences were observed between the 15Co-15Ni and 30Co samples since the reduction took place at 240 ºC in both cases. As revealed earlier, the simultaneous deposition of cobalt and nickel active phases on the surface of the alumina support resulted in the partial insertion of Ni^{2+} cations into the lattice of Co_3O_4. This nickel doping led to the formation of Ni-Co mixed oxides with a structural configuration that tended to be similar to that of nickel cobaltite. In this sense, the similarity between the reduction traces, in terms of onset reduction temperature (175-200 ºC), peak reduction temperatures at 280 and 380 °C and narrowing of the window of the reduction process at low temperatures, of the bimetallic catalysts and that of the as-synthesised $NiCo_2O_4$ bulk sample, indicated that this new substoichiometric mixed oxide phase could be partially formed.

The overall H_2 uptake of the bimetallic catalysts, which was divided into two contributions depending on the reduction temperature window, namely 175-500 °C and 500-950 °C, are listed in Table 3. The total consumption was found to be considerably larger (5.8 and 5.7 mmol g^{-1} for 25Co-5Ni and 20Co-10Ni, respectively) with respect to that of the 30Co catalyst (5.2 mmol g^{-1}). In the case of the 15Co-15Ni sample, its uptake (5.2 mmol g^{-1}) was virtually identical to that of the monometallic 30Co sample. Interestingly, the H_2 uptake ratio at low and high temperatures increased from 0.6 over the monometallic 30Co catalyst to 0.8-1.0 over the bimetallic catalysts. Thus, the largest reducibility at low temperatures was found for the 25Co-5Ni sample (2.9 mmol H_2 g^{-1})

with the other two Co-Ni samples having a comparable behaviour with an uptake around 2.6 mmol H_2 g^{-1}. On one hand, the observed promotion of reducibility could be attributed to the lower formation of cobalt and/or nickel aluminate. EDX analysis showed that the relative amount of aluminate-like species decreased from 47% over the 30Co catalyst to 33% over the 25Co-5Ni and 20Co-10Ni catalysts but only to 44% over the 15Co-15Ni sample. On the other hand, in view of the notable advance in the reduction at low temperatures, the favoured formation of easily reducible $NiCo_2O_4$, as also evidenced by EDX, over the 25Co-5Ni and 20Co-10Ni samples was responsible for the increased H_2 consumption as well. In this regard, it is worth highlighting that the specific H_2 uptake of $NiCo_2O_4$ is 33.9 mmol H_2 g_{Co}^{-1}, markedly higher than that of Co_3O_4 (22.6 mmol H_2 g_{Co}^{-1}). In short, and more importantly, the H_2 uptake at low temperatures, which is indicative of the amount of easily reducible oxygen species related to $NiCo_2O_4$-like species, Co_3O_4, and NiO, increased from 2.0 mmol H_2 g^{-1} over the 30Co sample to 2.6-2.9 mmol H_2 g^{-1} over the bimetallic catalysts. The contribution of each species varied as a function of the Ni content. Thus, $NiCo_2O_4$-like species promoted the reducibility of the 25Co-5Ni catalyst while the redox behaviour of the 15Co-15Ni sample was controlled by its larger presence of NiO.

TABLE 3

As a complement of the H_2-TPR analysis, the reactivity of oxygen species present in the catalysts was evaluated by temperature-programmed reaction with methane in the absence of oxygen (CH_4-TPRe). This study can be envisaged to be more valuable than H_2-TPR analysis since, owing to the high reactivity of H_2, a more definite picture of the behaviour of the samples in methane oxidation may be described. In other words, the amount of oxygen species with a high activity in the target reaction could be better determined. The evolution of CO_2, CO and H_2 was monitored during the run by mass

spectrometry. In general, these profiles evidenced a two-step reaction process, as shown in Figure S8, Supplementary material. Unfortunately, the comparatively larger formation of CO_2 and CO (and H_2, not shown) above 500 °C made analysis of the obtained results in the low-temperature range rather difficult.

Accordingly, Figure 9 only shows the evolution of the CO_2 yield in the 200-550 ºC temperature window. As previously pointed out, this low-temperature reaction step was attributed to the complete oxidation of methane to CO_2 by lattice oxygen species bonded to Co^{3+} ions of $NiCo_2O_4$-like and/or Co_3O_4 species, as determined by XPS analysis. CO and H_2 were not detected during this process. Note that the amount of CO_2 produced by the complete oxidation reaction over the 30Ni sample was hardly observable. This low activity was connected to the reduced presence of highly dispersed Ni^{2+} cations. Secondly, the partial oxidation of methane took place above 525-550 °C (450 °C for the 30Ni sample), where methane was activated by low-mobility oxygen species bonded to Co^{2+} and Ni^{2+} ions from Co_3O_4 and NiO, giving rise to, in addition to CO_2, significant amounts of CO and H_2 [51]. It should be mentioned that this second reaction step was not noticed over the 30Co catalyst, which pointed to this only being able to take place at temperatures above 600 °C. Therefore, when comparing the profiles of the 30Co sample and those of the bimetallic samples, it was clear that the addition of nickel significantly improved the reactivity of the Co^{3+} cations. This led not only to an increase in the amount of evolved CO_2, and consequently in the amount of highly active oxygen species from 0.33 mmol O_2 g_{Me}^{-1} for the 30Co sample to 0.83 mmol O_2 g_{Me}^{-1} for the 25Co-5Ni sample (Table 2), but also a notable decrease in the peak temperature required for the occurrence of the complete oxidation reaction, from around 490 °C for the 30Co sample down to 420 °C for the 25Co-5Ni sample (Figure 9). The O_2 uptakes were estimated by integration of the profiles. The selected

557 threshold temperatures were 510, 515, 540 and 550 ºC for the 25Co-5Ni, 20Co-10Ni,
558 15Co-15Ni and 30Co samples, respectively.

559 FIGURE 9

560

561 *3.2. Behaviour of the Co-Ni catalysts in the oxidation of lean methane*

562 The corresponding light-off curves of the synthesised Co-Ni/Al_2O_3 catalysts operating
563 at 300 mL CH_4 g^{-1} h^{-1} are shown in Figure 10. Three consecutive light-off tests were
564 carried out for each catalyst. The second and third cycles were characterised by an
565 identical light-off curve. For this reason, the profiles included in Figure 10 are those
566 corresponding to the third experiment. All studied Co-based catalysts showed 100%
567 CO_2 selectivity in the whole temperature range. Appreciable amounts of carbon
568 monoxide were only detected over the 30Ni sample. This resulted in CO_2 selectivity
569 values of only around 90% in the 450-600 °C temperature range.

570 FIGURE 10

571 Both monometallic catalysts (30Co and 30Ni) resulted efficient for deep methane
572 oxidation. The cobalt sample showed a better performance at lower temperatures (below
573 500 °C). However, above 550 °C, temperature at which the two catalysts attained 50%
574 conversion to CO_2 (Table 4), their behaviour was virtually identical with an 82%
575 conversion at 600 °C. On the other hand, the three bimetallic Co-Ni catalysts performed
576 substantially better than their monometallic counterparts over the whole temperature
577 range with an advance in the combustion temperatures of about 50 °C. It was therefore
578 found that, for a total metal loading of 30%wt., the co-addition of cobalt and nickel was
579 suitable for producing highly active catalysts. The best results were obtained when the
580 nickel content was limited to 5-10%wt. These two samples, namely 25Co-5Ni and
581 20Co-10Ni, exhibited very close T_{50} values (495 and 500 °C, respectively). Slight

differences in behaviour were noticed as the 25Co-5Ni was more active at lower temperatures while the opposite occurred at high temperatures. A higher Ni loading (15%wt.) led to somewhat lower conversion values, with a T_{50} value of 510 °C. To provide further insights on the kinetic behaviour of the investigated catalysts, the reaction rate was estimated using the differential method at 425 °C, where conversion was below 20%. The corresponding results normalised to the total amount of metal are summarised in Table 4. Based on the values of the specific reaction rate, the activity decreased in the following order: 25Co-5Ni (3.3 mmol CH_4 g_{Me}^{-1} h^{-1}) > 20Co-10Ni (3.1 mmol CH_4 g_{Me}^{-1} h^{-1}) > 15Co-15Ni (2.9 mmol CH_4 g_{Me}^{-1} h^{-1}) > 30Co (1.7 mmol CH_4 g_{Me}^{-1} h^{-1}) > 30Ni (0.7 mmol CH_4 g_{Me}^{-1} h^{-1}). These values showed that the introduction of a relatively low amount of nickel was suitable for the design of improved alumina-supported cobalt catalysts for the oxidation of lean methane. Additional catalytic results were carried out a markedly higher weight hourly space velocity (450mL CH_4 g^{-1} h^{-1}, 45,000 h^{-1}) in order to better evidence an eventually more marked difference in behaviour of the three Co-Ni catalysts. Results are included in Figure 11, while the corresponding kinetic results are listed in Table 4. It was found that T_{50} varied from 500 ºC over the 25Co-5Ni samples to 535 ºC and 545 ºC over the 20Co-5Ni and 15Co-15Ni samples, respectively, under these more demanding conditions. This difference in activy was also evidenced by the values of the specific reaction rate at 425 °C, since the 25Co-5Ni catalyst achieved 3.0 mmol CH_4 g_{Me}^{-1} h^{-1} while the 20Co-10Ni and 15Co-15Ni catalysts only attained 1.9 and 1.2 mmol CH_4 g_{Me}^{-1} h^{-1}, respectively.

TABLE 4

The superior activity of the bimetallic catalysts was connected with their better reducibility and higher mobility of oxygen species. This relationship was evidenced

607 when the specific reaction rate was compared with the surface molar composition
608 (Co^{3+}/Co^{2+} and O_{ads}/O_{latt} molar ratios) determined by XPS and the specific O_2
609 consumption at low temperatures derived from the CH_4-TPRe runs. As shown in Figure
610 5, a direct correlation was found, thus revealing that the most active catalysts (the
611 bimetallic Co-Ni samples at both 300 and 450 mL CH_4 g^{-1} h^{-1}) exhibited larger O_2
612 consumption values with respect to the less active monometallic catalysts. Note that
613 these catalysts also showed higher H_2 uptakes in H_2-TPR analysis, as shown in Figure
614 S9, Supplementary material. Moreover, the influence of the O_{ads}/O_{latt} molar ratio on the
615 specific activity showed that the origin of the active oxygen species was the spinel
616 lattice, and that a higher Co^{3+}/Co^{2+} molar ratio favoured their presence. In this sense, the
617 best catalyst composition (25Co-5Ni) was characterised by the highest values of both
618 O_2 consumption, and Co^{3+}/Co^{2+} molar ratio, thereby revealing that its superior
619 reducibility and enhanced lattice oxygen mobility were responsible for its promising
620 catalytic behaviour. In addition to the amount of active sites, which was considered to
621 be proportional to measure O_2 uptake, its reactivity at low temperature was also
622 important, expressed as the onset temperature in the CH_4-TPRe run (Figure S10,
623 Supplementary material). The main reason behind this improved activity seemed to be
624 the insertion of Ni^{2+} ions in the Co_3O_4 lattice and the subsequent formation of a
625 $NiCo_2O_4$-like spinel to some extent combined with a notable presence of Co_3O_4 and a
626 minimal contribution of NiO and metal aluminates. The high efficiency of $NiCo_2O_4$ as
627 an active phase for the oxidation of CO [52], soot [53] and light hydrocarbons [54] has
628 already been reported elsewhere. Moreover, nickel cobaltite has shown an excellent
629 behaviour for the oxidation of lean methane as pointed out by Tao el at. [55] and Wang
630 et al. [56]. Both studies evidenced the role played by surface lattice oxygen species in
631 the formation of CH_3O species after dissociation of first C-H in methane. Figure S11,

Supplementary material, compares the light-off curves of the as-synthesised bulk $NiCo_2O_4$ and Co_3O_4 catalysts evaluated under the same reaction conditions (300 mL g^{-1} h^{-1}). It was noticed that both profiles were virtually identical at low temperature, while the bulk nickel cobaltite was slightly more active above 450 °C. The specific reaction rates of both samples, calculated at 350 °C, were comparable when they were calculated based on the total metallic loading (1.1 mmol CH_4 g_{Me}^{-1} h^{-1}). However, when the specific reaction rates were estimated per gram of cobalt, $NiCo_2O_4$ exhibited a significantly higher value (1.7 mmol CH_4 g_{Co}^{-1} h^{-1}) than Co_3O_4 (1.1 mmol CH_4 g_{Co}^{-1} h^{-1}). Note that whilst the cobalt content of Co_3O_4 was 73%wt., it was 49%wt. for $NiCo_2O_4$. That is, even though both active phases were equally active, the $NiCo_2O_4$ phase required a smaller amount of cobalt to reach the same level of conversion. Therefore, for a given amount of cobalt, a higher fraction of active phase could be obtained if this were in the form of $NiCo_2O_4$, rather than Co_3O_4. As a result, the formation of the former oxide allowed for a more efficient use of the deposited cobalt.

On the other hand, the apparent activation energy of the catalysts was estimated by the integral method. A kinetic equation with a first pseudo-order for methane and a zeroth pseudo-order for oxygen, in accordance with a Mars–van Krevelen kinetics in excess of oxygen, was employed for this calculation [57,58]. The resulting plots from the linearised Arrhenius equation are depicted in Figure S12, Supplementary material, while the apparent activation energy and the pre-exponential factor of the various catalysts are summarised in Table 4. The values for the 30Co and 25Co-5Ni catalysts were relatively similar (82-84 kJ mol^{-1}) and close to those shown by both bulk Co_3O_4 and $NiCo_2O_4$ (75 and 76 kJ mol^{-1}, respectively). While having a comparable apparent activation energy, the higher activity of the 25Co-5Ni sample could be explained by its higher pre-exponential factor ($7.1 \cdot 10^6$ s^{-1}) with respect to the 30Co catalyst ($4.8 \cdot 10^6$ s^{-1}).

This difference suggested the presence of a larger number of active sites on the surface of the bimetallic sample. Over the bimetallic samples with a higher Ni content (20Co-10Ni and 15Co-15Ni) the values were significantly higher (89-91 kJ mol^{-1}). This finding was coherent with the contribution of less active NiO species, which were more abundant on these catalysts, as revealed by STEM-HAADF-EDX. In fact, the apparent activation energy of the 30Ni sample with NiO as the only active species was remarkably higher (128 kJ mol^{-1}). To sum up, the kinetic analysis of the behaviour was in accordance with the nature and intrinsic activity of each oxide phase present in a given sample, which in turn strongly depended on the catalyst composition.

TABLE 4

Finally, the stability of the most active catalyst (25Co-5Ni) with prolonged time on stream was investigated at a constant temperature of 550 °C for a total reaction time of 150 hours. The reaction atmosphere was switched every 25 hours between dry (1%CH_4/10%O_2/89%N_2) and humid (1%CH_4/10%O_2/10%H_2O/79%N_2) conditions to enable the additional analysis of the influence of hydrothermal ageing. The results included in Figure 11 revealed that the catalyst underwent an initial thermal deactivation where the conversion dropped from 70% to 61%. Then, conversion stabilised after 15 hours on stream. The addition of water to the feedstream provoked a drastic decrease in conversion, down to 25%, which further decreased to a stable value of 21%. The subsequent cut-off of steam after 50 hours on stream enabled a partial recovery of the conversion, up to 48%, thus showing that water also induced some irreversible deactivation over this type of catalyst. This trend was also observed at longer reaction time intervals, with the conversion continuously decreasing after each of the successive humid cycles. This inhibiting effect by water has also been found over noble metal-based (Pd and Pt) catalysts. For instance, Mihai et al. [59] observed a significant

682 inhibition of a Pd/Al_2O_3 catalyst supported on a cordierite monolith operating at
683 30,330 h^{-1} when 5%vol. of steam was added to the feed stream, with an increase of T_{50}
684 of 200 °C with respect to dry operation. Velin et al. [60] reported a dramatic loss of
685 activity of a PdO/Al_2O_3 catalyst under wet conditions (32,000 h^{-1}) over a period of 5
686 hours, while only a small loss was noticed under dry conditions over a period of 24
687 hours. As for Pt catalysts, Abbasi et al. [61] reported an irreversible loss of the catalytic
688 activity of a Pt-washcoated monolith after exposure to 5%vol. of water operating at
689 around 28,000 h^{-1}. On the other hand, Nassiri et al. [62] observed that a monometallic Pt
690 catalyst supported over γ-Al_2O_3 showed a very low conversion (<10%) in the 400-
691 550 °C temperature range when 5%vol.H_2O was fed into the stream at 27,200 h^{-1}. When
692 water admission was cut off, the conversion only increased very slightly.
693 The characterisation of the used catalyst after the whole stability test revealed that the
694 observed deactivation was due to a notable decrease in specific surface area (from 113
695 to 97 m^2 g^{-1}) and pore volume (from 0.35 to 0.31 cm^3 g^{-1}), along with an increase in the
696 crystallite size of the spinel phase (from 21 to 32 nm). Note that the absence of
697 carbonaceous species was verified by XRD and dynamic thermogravimetry under
698 oxidative conditions coupled to mass spectrometry. Likewise, the availability of active
699 oxygen species seemed not to be significantly affected by the long operation time or by
700 the presence of water vapour in the feedstream. More specifically, O_2 consumption at
701 low temperatures of the used catalyst (0.84 mmol g_{Me}^{-1}), as evaluated by CH_4-TPRe,
702 was identical to that of its fresh counterpart (0.83 mmol g_{Me}^{-1}), although it was noted
703 that the low temperature reaction event for the used sample shifted around 50 °C
704 towards higher temperatures. Accordingly, this shift may be attributed to the loss of
705 specific surface area and the growth of the spinel crystallite, but not to a loss of
706 reducibility itself.

FIGURE 11

4. Conclusions

A series of bimetallic cobalt-nickel catalysts supported over alumina was synthesised by basic co-precipitation, extensively characterised (N_2 physisorption, WDXRF, XRD, Raman spectroscopy, XPS, STEM-HAADF coupled to EELS and EDX, HRTEM, H_2-TPR and CH_4-TPRe) and investigated for complete oxidation of methane under lean conditions. The total metallic loading was 30%wt., whilst the nickel loading was varied between 5-15%wt. For comparative purposes, additional reference catalysts including supported monometallic samples and bulk NiO, Co_3O_4 and $NiCo_2O_4$ oxides, were also prepared following the same synthesis route. We then examined the structural evolution of bimetallic catalysts with different compositions as well as their catalytic performance at different temperatures and during extended time on stream under both dry and humid conditions.

The resulting Co-Ni catalysts exhibited good textural properties, with only a slight loss of specific surface (12-19%) with respect to the bare alumina. The metal oxides were preferentially deposited on the largest pores of the support. Combined results from XRD and Raman spectroscopy showed that the addition of nickel was efficient for inhibiting the formation of $CoAl_2O_4$, which is an inactive cobalt phase. As pointed out by chemical mapping by EELS and spot analysis by EDX, in addition to Co_3O_4, the formation of $NiCo_2O_4$-like owing to the partial insertion of Ni^{2+} cation into the lattice of Co_3O_4 was favoured when relatively low amounts of nickel were incorporated. In contrast, segregated NiO was observed for Ni loadings between 10-15%wt as simultaneously evidenced by XRD and HRTEM.

731 XPS confirmed all these findings since an increase in the Co^{3+}/Co^{2+} molar ratio was
732 noticed for the 25Co-5Ni catalyst, which was coherent with the presence of nickel
733 cobaltite, where most cobalt species were as Co^{3+}, and the preferential abundance of
734 Ni^{2+} species belonging to $NiCo_2O_4$ at the expense of NiO and $NiAl_2O_4$. The high Co^{3+}
735 concentration at the surface level was in turn connected to an increased presence of
736 lattice oxygen species. The strong cobalt-nickel interaction that resulted in the formation
737 of $NiCo_2O_4$, instead of Co_3O_4 and $CoAl_2O_4$, promoted the redox properties of the
738 resulting Co-Ni samples. Thus, when compared with the reference monometallic cobalt
739 catalyst, the reduction onset temperature was noticeably shifted to lower temperatures
740 and the specific H_2 uptake in the low temperature range increased to a considerable
741 extent. Furthermore, the higher mobility of active oxygen species for the Co-Ni
742 catalysts, and particularly for the 25Co-5Ni sample, was also evidenced by temperature-
743 programmed reaction with methane.
744 A noticeably higher efficiency for lean methane combustion in terms of both specific
745 reaction rate and reaction temperatures needed for full methane conversion to CO_2 was
746 found over the bimetallic catalysts in comparison with their monometallic counterparts.
747 In line with the characterisation results, its superior activity was associated with their
748 better reducibility and higher mobility of oxygen species. The optimal catalyst
749 composition was that given by the 25Co-5Ni catalyst, which suitably combined the co-
750 presence of highly active $NiCo_2O_4$ and Co_3O_4 at the expense of NiO, $CoAl_2O_4$ and
751 $NiAl_2O_4$. While the behaviour of this catalyst was relatively stable under dry conditions,
752 the presence of water (10%vol.) provoked a marked partially reversible decrease in
753 conversion. After operation for 150 hours under cycled dry/humid conditions,
754 significant changes in surface area and sintering were noticed. Although these

phenomena did not affect the amount of available oxygen species, their mobility was appreciably inhibited.

Acknowledgments

This research was funded by the Ministry of Economy and Competitiveness (CTQ2016-80253-R AEI/FEDER, UE), Basque Government (IT1297-19) and the University of The Basque Country UPV/EHU (PIF15/335). The author wish to thank the technical and human support provided by SGIker (UPV/EHU) and the Advanced Microscopy Laboratory of the University of Zaragoza.

References

[1] European Environment Agency (EEA), (2018), Briefing no. 15/2018, Progress of EU transport sector towards its environment and climate objectives.

[2] V.V. Georgatzi, Y. Stamboulis, A. Vetsikas, Econ. Anal. Policy 65 (2020) 11-20.

[3] M.I. Khan, T. Yasmin, A. Shakoor, Renew. Sust. Energ. Rev. 51 (2015) 785-797.

[4] Z. Yuan, X. Ou, T. Peng, X. Yan, Appl. Energ. 253 (2019) 113472.

[5] D.J.G. Crow, P. Balcombe, N. Brandon, A.D. Hawkes, Sci. Total Environ. 668 (2019) 1242-1258.

[6] A. Yousefi, H. Guo, M. Birouk, B. Liko, Appl. Energ. 242 (2019) 216-231.

[7] S. Trivedi, R. Prasad, J. Environ. Chem. Eng. 4 (2016) 1017-1028.

[8] G. Ercolino, P. Stelmachowski, G. Grzybek, A. Kotarba, S. Specchia, Appl. Catal. B Environ. 206 (2017) 712-725.

[9] R.F.K. Gunnewiek, C.F. Mendes, R.H.G.A. Kiminami, Adv. Powder Technol. 27 (2016) 1056-1061.

[10] C. Wang, W. Hua, G. Chai, C. Zhang, Y. Guo, Catalysts 9 (2019) 408.

780 [11] J. Park, S. Yeo, T. Kang, I. Heo, K. Lee, T. Chang, Fuel 212 (2018) 77-87.
781 [12] J.A. Onrubia-Calvo, B. Pereda-Ayo, U. De-La-Torre, J.R. González-Velasco,
782 Catal. Today 333 (2019) 208-218.
783 [13] M.A. Ulla, R. Spretz, E. Lombardo, W. Daniell, H. Knözinger, Appl. Catal. B
784 Environ. 29 (2001) 217-229.
785 [14] W.K. Jozwiak, E. Szubiakiewicz, J. Góralski, A. Klonkowski, T. Paryjczak,
786 Kinet. Catal. 45 (2004) 247-255.
787 [15] A. Rokicińska, M. Drozdek, B. Dudek, B. Gil, P. Michorczyk, D. Brouri, S.
788 Dzwigaj, P. Kuśtrowski, Appl. Catal. B Environ. 212 (2017) 59-67.
789 [16] S. Gudyka, G. Grzybek, J. Grybos, P. Indyka, B. Leszczynski, A. Kotarba, Z.
790 Sojka, Appl. Catal. B Environ. 201 (2017) 339-347.
791 [17] G. Grzybek, K. Ciura, J. Grybos, P. Indyka, A. Davó-Quiñonero, D. Lozano-
792 Castelló, A. Bueno-Lopez, A. Kotarba, Z. Sojka, J. Phys. Chem. C 123 (2019)
793 20221-20232.
794 [18] L.F. Liotta, G. Pantaleo, A. Macaluso, G. Di Carlo, G. Deganello, Appl. Catal. A
795 Gen. 245 (2003) 167-177.
796 [19] S. Park, G. Kwak, Y. Lee, K. Jun, Y.T. Kim, Bull. Korean Chem. Soc. 39 (2018)
797 540-547.
798 [20] A. Choya, B. de Rivas, J.R. González-Velasco, J.I. Gutiérrez-Ortiz, R. López-
799 Fonseca, Appl. Catal. A Gen. 582 (2019).
800 [21] A. Choya, B. de Rivas, J.I. Gutiérrez-Ortiz, R. López-Fonseca, Catalysts 8 (2018)
801 427.
802 [22] A. Choya, B. de Rivas, J.R. González-Velasco, J.I. Gutiérrez-Ortiz, R. López-
803 Fonseca, Appl. Catal. B Environ. 237 (2018) 844-854.

804 [23] A. Aranzabal, J.A. González-Marcos, J.L. Ayastuy, J.R. González-Velasco,
805 Chem. Eng. Sci. 61 (2006) 3564-3576.
806 [24] Eurokin. http://eurokin.org/, 2018 (accessed 21 April 2020).
807 [25] J.L. Ewbank, L. Kovarik, C.C. Kenvin, C. Sievers, Green Chem. 16 (2014) 885-
808 896.
809 [26] M. Gil-Calvo, C. Jiménez-González, B. de Rivas, J.I. Gutiérrez-Ortiz, R. López-
810 Fonseca, Appl. Catal. B Environ. 209 (2017) 128-138.
811 [27] I. Zacharaki, C.G. Kontoyannis, S. Boghosian, A. Lycourghiotis, C. Kordulis,
812 Catal. Today 143 (2009) 38-44.
813 [28] Y.J. Wong, M.K. Koh, N.F. Khairudin, S. Ichikawa, Y. Morikawa, A.R.
814 Mohamed, ChemCatChem 11 (2019) 5593-5605.
815 [29] X. Zhang, M. Zhao, Z. Song, H. Zhao, W. Liu, J. Zhao, Z. Ma, Y. Xing, New J.
816 Chem. 43 (2019) 10868-10877.
817 [30] V. D'Ippolito, G.B. Andreozzi, D. Bersani, P.P. Lottici, J. Raman Spectrosc. 46
818 (2015) 1255-1264.
819 [31] X. Jiang, Y. Ma, Y. Chen, Y. Li, Q. Ma, Z. Zhang, C. Wang, Y. Yang,
820 Spectrochim. Acta Part A Mol. Biomol. Spectrosc. 190 (2018) 61-67.
821 [32] S. Visweswaran, R. Venkatachalaphy, M. Haris, R. Murugesan, Appl. Phys. A
822 Mater., 126 (2020) 524.
823 [33] G. George, S. Anandhan, RSC Adv. 4 (2014) 62009-62020.
824 [34] R. Benrabaa, A. Barama, H. Boukhlouf, J. Guerrero-Caballero, A. Rubbens, E.
825 Bordes-Richard, A. Löfberg, R.-. Vannier, Int. J. Hydrogen Energy 42 (2017)
826 12989-12996.
827 [35] P. Stelmachowski, A.H.A. Monteverde Videla, K. Ciura, S. Specchia, Int. J.
828 Hydrogen Energy 42 (2017) 27910-27918.

[36] C. Zhang, Y. Wang, G. Li, L. Chen, Q. Zhang, D. Wang, X. Li, Z. Wang, Appl. Surf. Sci. 532 (2020) 147320.

[37] J. Yang, H. Liu, W.N. Martens, R.L. Frost, J. Phys. Chem. C 114 (2010) 111-119.

[38] I. Preda, R.J.O. Mossanek, M. Abbate, L. Alvarez, J. Méndez, A. Gutiérrez, L. Soriano, Surf. Sci. 606 (2012) 1426-1430.

[39] Y. Wan, J. Chen, J. Zhan, Y. Ma, J. Environ. Chem. Eng. 6 (2018) 6079-6087.

[40] J. Dupin, D. Gonbeau, P. Vinatier, A. Levasseur, Phys. Chem. Chem. Phys. 2 (2000) 1319-1324.

[41] K. Zeng, X. Li, C. Wang, Z. Wang, P. Guo, J. Yu, C. Zhang, X.S. Zhao, J. Colloid Interf. Sci. 572 (2020) 281-296.

[42] X. Shi, S.L. Bernasek, A. Selloni, J. Phys. Chem C 120 (2016) 14892-14898.

[43] Y. Gou, X. Liang, B. Chen, J. Alloys Compd. 574 (2013) 181-187.

[44] Z. Ren, Z. Wu, W. Song, W. Xiao, Y. Guo, J. Ding, S.L. Suib, P-X. Gao, Appl. Catal. B: Environmental 180 (2016) 150-160.

[45] D. Delgado, R. Sanchís, J.A. Cecilia, E. Rodríguez-Castellón, A. Caballero, B. Solsona, J.M.L. Nieto, Catal. Today 333 (2019) 10-16.

[46] G. Garbarino, S. Chitsazan, T.K. Phung, P. Riani, G. Busca, Appl. Catal. A Gen. 505 (2015) 86-97.

[47] L.F. Liotta, G. Di Carlo, G. Pantaleo, A.M. Venezia, G. Deganello, Appl. Catal. B Environ. 66 (2006) 217-227.

[48] J. González-Prior, R. López-Fonseca, J.I. Gutiérrez-Ortiz, B. de Rivas, Appl. Catal. B Environ. 222 (2018) 9-17.

[49] Y. Wang, C. Wang, M. Chen, J. Hu, Z. Tang, D. Liang, W. Cheng, Z. Yang, J. Wang, H. Zhang, Fuel 279 (2020) 118449.

[50] G. Zou, Y. Xu, S. Wang, M. Chen, W. Shangguan, Catal. Sci. Technol. 5 (2015) 1084-1092.

[51] Z. Chen, S. Wang, W. Liu, X. Gao, D. Gao, M. Wang, S. Wang, Appl. Catal. A Gen. 525 (2016) 94-102.

[52] S. Trivedi, R. Prasad, Asia-Pac. J. Chem. Eng. 12 (2017) 440-453.

[53] M. Zhao, J. Deng, J. Liu, Y. Li, J. Liu, Z. Duan, J. Xiong, Z. Zhao, Y. Wei, W. Song, Y. Sun, ACS Catal. 9 (2019) 7548-7567.

[54] Y. Huang, W. Fan, B. Long, H. Li, W. Qiu, F. Zhao, Y. Tong, H. Ji, J. Mater. Chem. A 4 (2016) 3648-3654.

[55] F.F. Tao, J.J. Shan, L. Nguyen, Z. Wang, S. Zhang, L. Zhang, Z. Wu, W. Huang, S. Zeng, P. Hu, Nat. Commun. 6 (2015) 7798.

[56] T. Wang, J. Wang, Y. Sun, Y. Duan, S. Sun, X. Hu, S. Xie, Y. Due, C. Wang, Z.J. Xu, Appl. Catal. B Environ. 256 (2019) 117844.

[57] F. Zasada, J. Janas, W. Piskorz, M. Gorczynska, Z. Sojka, ACS Catal. 7 (2017) 2853-2867.

[58] E. Genty, S. Siffert, R. Cousin, Catal. Today 333 (2019) 28-35.

[59] O. Mihai, G. Smedler, U. Nylén, M. Olofsson, L. Olsson, Catal. Sci. Technol. 7 (2017) 3084.

[60] P. Velin, M. Ek, M. Skoglundh, A. Schaefer, A. Raj, D. Thompsett, G. Smedler, P.-A. Carlsson, J. Phys. Chem. C 123 (2019) 25724-25737.

[61] R. Abbasi, L. Wu, S.E. Wanke, R.E. Hayes, Chem. Eng. Res. Des. 90 (2012) 1930-1942.

[62] H. Nassiri, R.E. Hayes, N. Semagina, Chem. Eng. Sci. 186 (2018) 44-51.

CAPTIONS FOR TABLES AND FIGURES

Table 1. Composition and textural and structural properties of the Co-Ni catalysts.

Table 2. Surface composition of the Co-Ni catalysts.

Table 3. Results from the H_2-TPR and CH_4-TPRe analysis of the Co-Ni catalysts.

Table 4. Kinetic results of the Co-Ni catalysts.

Figure 1. Close-up view of the XRD profiles of the Co-Ni catalysts in the 35-39° 2θ range.

Figure 2. Raman spectra of the Co-Ni catalysts in the 150-900 cm^{-1} range.

Figure 3. XPS profiles of the Co-Ni catalysts (a) Co2p, b) Ni2p and c) O1s).

Figure 4. Evolution of the $Co2p_{3/2}$ main signal and the Ni^{2+} signal from a spinel lattice for the Co-Ni catalysts.

Figure 5. Relationship between the surface composition (XPS) and O_2 consumption at low temperature (CH_4-TPRe) with the activity of the Co-Ni catalysts at 300 mL CH_4 g^{-1} h^{-1} (a) and 450 mL CH_4 g^{-1} h^{-1} (b).

Figure 6. STEM-HAADF images and EELS maps of the Co-Ni catalysts. (Red) cobalt and (blue) nickel.

Figure 7. Oxide phase distribution over the Co-Ni catalysts as determined by STEM-HAADF coupled to EDX.

Figure 8. H_2-TPR profiles of the Co-Ni catalysts in the 50-900 ºC temperature range.

Figure 9. Close-up view of the CH_4-TPRe profiles of the Co-Ni catalysts in the 200-550 °C temperature range. For the 30Ni sample, only the results corresponding to the 200-430 °C temperature range are plotted.

Figure 10. Light-off curves of the Co-Ni catalysts in the 200-600 ºC temperature range at 300 mL CH_4 g^{-1} h^{-1}.

Figure 11. Light-off curves of the Co-Ni catalysts in the 200-600 ºC temperature range at 450 mL CH_4 g^{-1} h^{-1}.

Figure 12. Evolution of methane conversion with time on stream over the 25Co-5Ni catalyst under cycled dry/humid conditions at 550 ºC and 300 mL CH_4 g^{-1} h^{-1}.

Catalyst	Co, %wt.	Ni, %wt.	Ni/Co molar ratio	S_{BET}, $m^2\ g^{-1}$	V_{pore}, $cm^3\ g^{-1}$	Pore size distribution maxima, Å	$D_{Co\text{-}spinel}$, nm	D_{NiO}, nm	Cell parameter, Å
Al_2O_3	-	-	-	139	0.56	90, 150	-	-	-
30Co	27.0	-	0.0	108	0.29	90	29	-	8.0960
25Co-5Ni	23.2	4.8	0.2	113	0.35	90	21	-	8.1037
20Co-10Ni	18.1	9.4	0.5	123	0.38	90	22	19	8.1068
15Co-15Ni	13.3	14.0	1.1	117	0.40	90, 125, 340	23	18	8.1087
30Ni	-	27.1	-	128	0.37	90	-	14	-
$NiCo_2O_4$	49.0	24.4	0.5	11	0.06	320	17	-	8.1232

TABLE 1

Catalyst	Ni, %wt.	Co, %wt.	Al, %wt.	Co^{3+}/Co^{2+} molar ratio	O_{ads}/O_{latt} molar ratio	Ni^{2+}(NiO)/Ni^{2+}(spinel) molar ratio	Ni^{3+}/Ni^{2+} molar ratio
30Co	-	22.6 (27.9)	32.1 (37.0)	0.69	1.41	-	-
25Co-5Ni	8.2 (4.8)	25.4 (23.2)	22.7 (33.0)	1.20	0.94	0.26	0.13
20Co-10Ni	18.6 (9.4)	22.7 (18.1)	22.5 (33.6)	1.11	1.04	0.55	0.24
15Co-15Ni	27.9 (14.0)	14.8 (13.3)	21.7 (33.7)	0.95	1.10	0.93	0.29
30Ni	40.6 (27.1)	-	22.1 (34.7)	-	1.54	0.71	0.30
$NiCo_2O_4$	31.5 (24.4)	38.8 (49.0)	-	2.10	0.43	0.82	0.39

Values in brackets correspond to the metallic loading as determined by WDXRF.

TABLE 2

	H_2-TPR			CH_4-TPRe
Catalyst	Low temperature H_2 uptake, mmol g^{-1}	High temperature H_2 uptake, mmol g^{-1}	Total H_2 uptake, mmol g^{-1}	Low temperature O_2 consumption, mmol g_{Me}^{-1}
30Co	2.01	3.16	5.18	0.33
25Co-5Ni	2.86	2.96	5.82	0.83
20Co-10Ni	2.58	3.13	5.71	0.71
15Co-15Ni	2.64	2.52	5.16	0.64
30Ni	1.44	2.97	4.42	0.13
$NiCo_2O_4$	16.39	0.26	16.65	1.72

TABLE 3

Catalyst	T_{50}, °C	Specific reaction rate, mmol CH_4 g_{Me}^{-1} h^{-1}	Apparent activation energy, kJ mol^{-1}	$k_0(x10^6)$, s^{-1}	T_{50}, °C	Specific reaction rate, mmol CH_4 g_{Me}^{-1} h^{-1}	Apparent activation energy, kJ mol^{-1}	$k_0(x10^6)$, s^{-1}
30Co	550	1.7	82 ± 2	4.7 ± 0.1	n.d.	n.d.	n.d.	n.d.
25Co-5Ni	500	3.3	84 ± 2	7.2 ± 0.2	500	3.0	85 ± 1	4.7± 0.1
20Co-10Ni	500	3.1	89 ± 1	8.0 ± 0.1	535	1.9	89 ± 1	5.5 ± 0.2
15Co-15Ni	510	2.9	91 ± 2	7.4 ± 0.2	545	1.2	92 ± 1	3.5± 0.1
30Ni	555	0.7	128 ± 3	0.1 ± 0.02	n.d.	n.d.	n.d.	n.d.

n.d.: not determined

TABLE 4

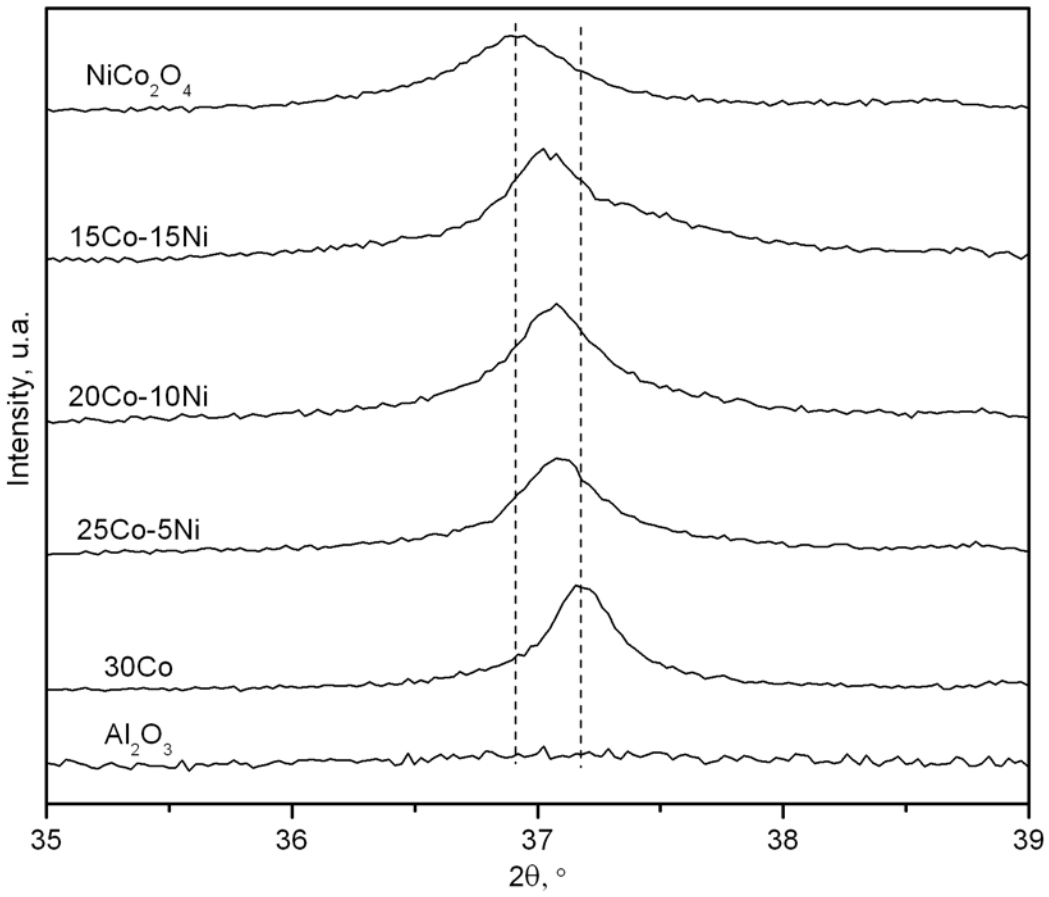
NiCo2O4
15Co-15Ni
20Co-10Ni
25Co-5Ni
30Co
Al2O3
Intensity, u.a.
35
36
37
38
39
2θ, °

FIGURE 1

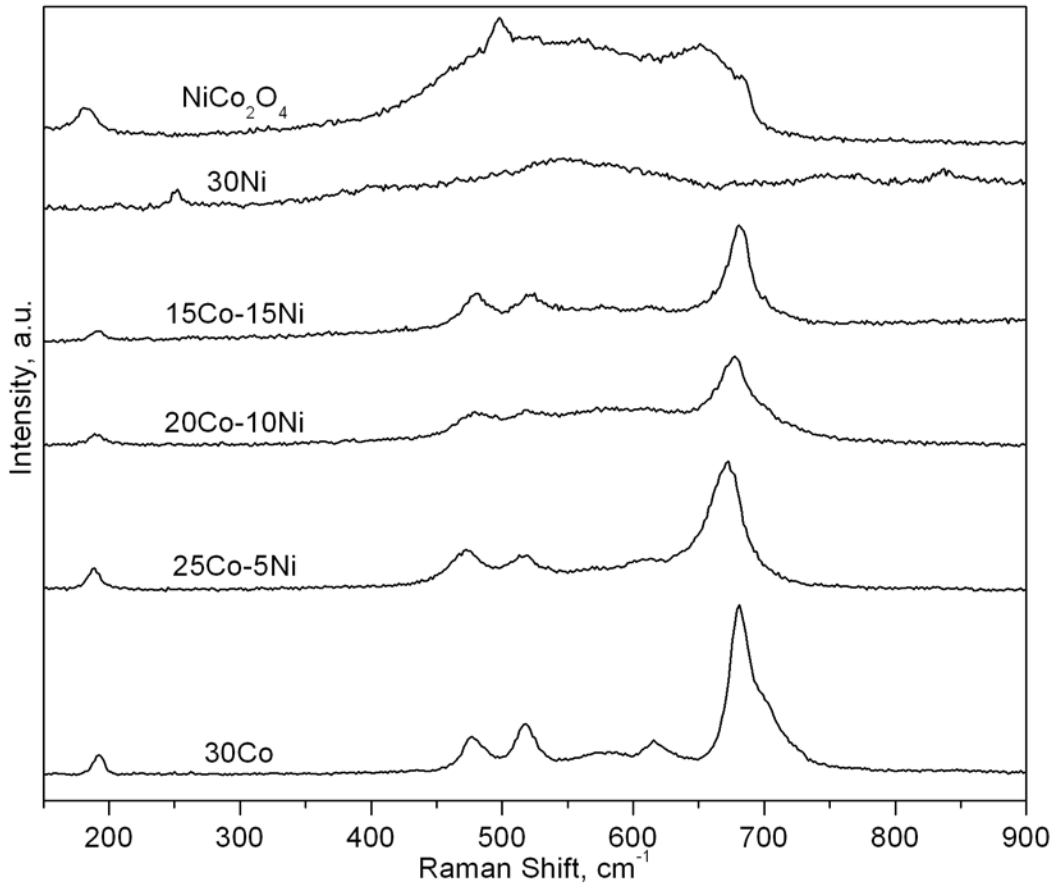
NiCo2O4
30Ni
15Co-15Ni
20Co-10Ni
25Co-5Ni
30Co
Intensity, a.u.
200
300
400
500
600
700
800
900
Raman Shift, cm-1

FIGURE 2

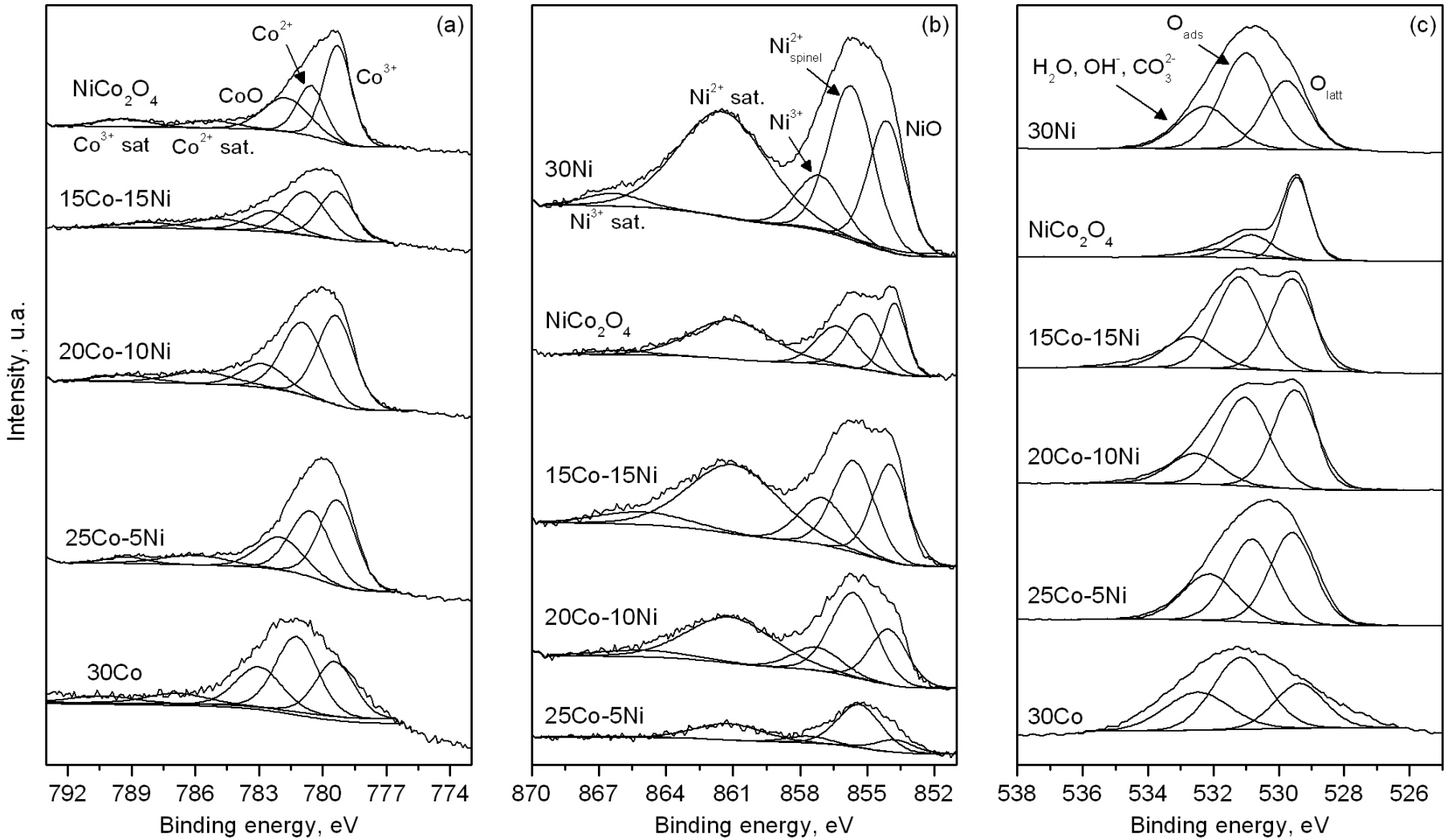
(a)
Co2+
Co3+
NiCo2O4
CoO
Co3+ sat
Co2+ sat.
15Co-15Ni
20Co-10Ni
25Co-5Ni
30Co
Intensity, u.a.
792 789 786 783 780 777 774
Binding energy, eV
(b)
Ni2+spinel
Ni2+ sat.
Ni3+
NiO
30Ni
Ni3+ sat.
NiCo2O4
15Co-15Ni
20Co-10Ni
25Co-5Ni
870 867 864 861 858 855 852
Binding energy, eV
(c)
Oads
H2O, OH-, CO32-
Olatt
30Ni
NiCo2O4
15Co-15Ni
20Co-10Ni
25Co-5Ni
30Co
538 536 534 532 530 528 526
Binding energy, eV

FIGURE 3

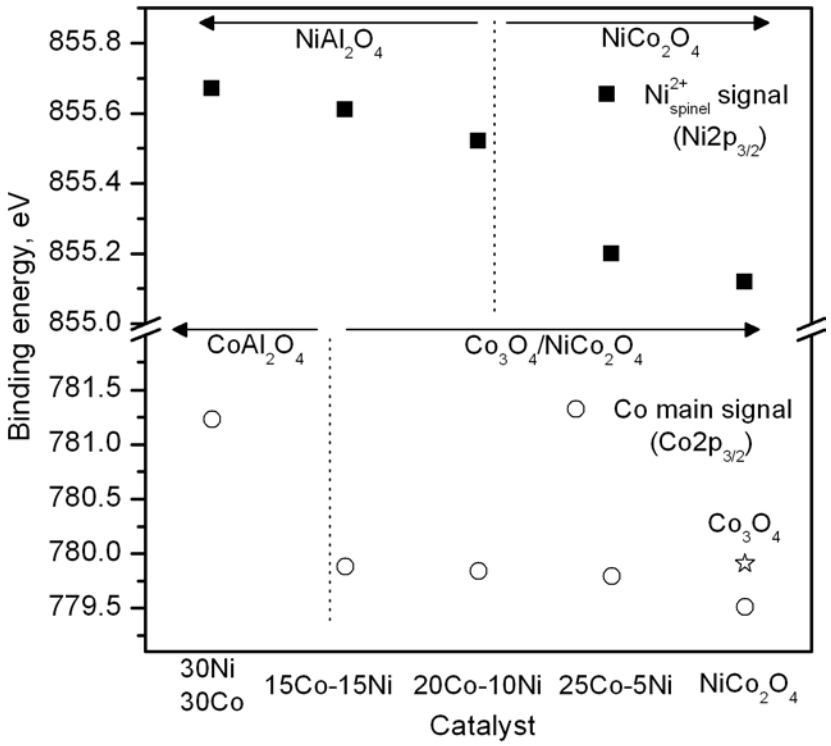
855.8
855.6
855.4
855.2
855.0
781.5
781.0
780.5
780.0
779.5
Binding energy, eV
NiAl2O4
NiCo2O4
Ni2+spinel signal
(Ni2p3/2)
CoAl2O4
Co3O4/NiCo2O4
Co main signal
(Co2p3/2)
Co3O4
30Ni
30Co
15Co-15Ni
20Co-10Ni
25Co-5Ni
NiCo2O4
Catalyst

FIGURE 4

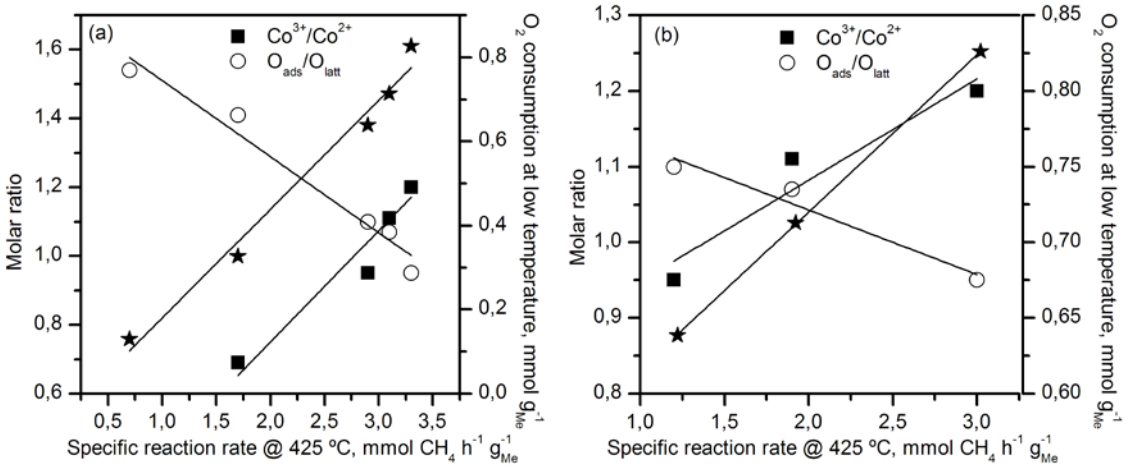
(a)
Co3+/Co2+
Oads/Olatt
Molar ratio
O2 consumption at low temperature, mmol gMe-1
Specific reaction rate @ 425 °C, mmol CH4 h-1 gMe-1
(b)
Co3+/Co2+
Oads/Olatt
Molar ratio
O2 consumption at low temperature, mmol gMe-1
Specific reaction rate @ 425 °C, mmol CH4 h-1 gMe-1

FIGURE 5

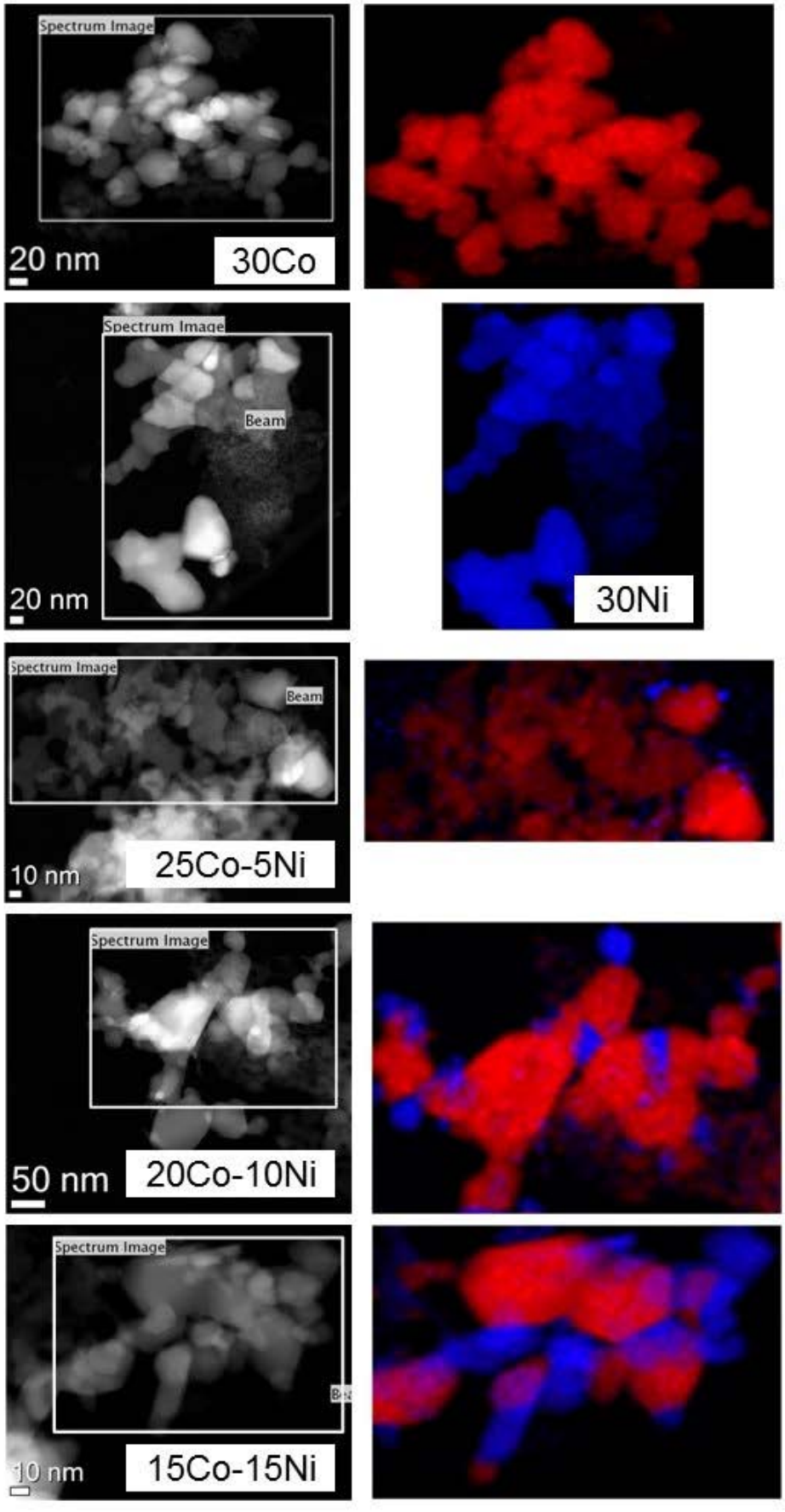
Spectrum Image
20 nm
30Co
Spectrum Image
Beam
20 nm
30Ni
Spectrum Image
Beam
10 nm
25Co-5Ni
Spectrum Image
50 nm
20Co-10Ni
Spectrum Image
10 nm
15Co-15Ni

FIGURE 6

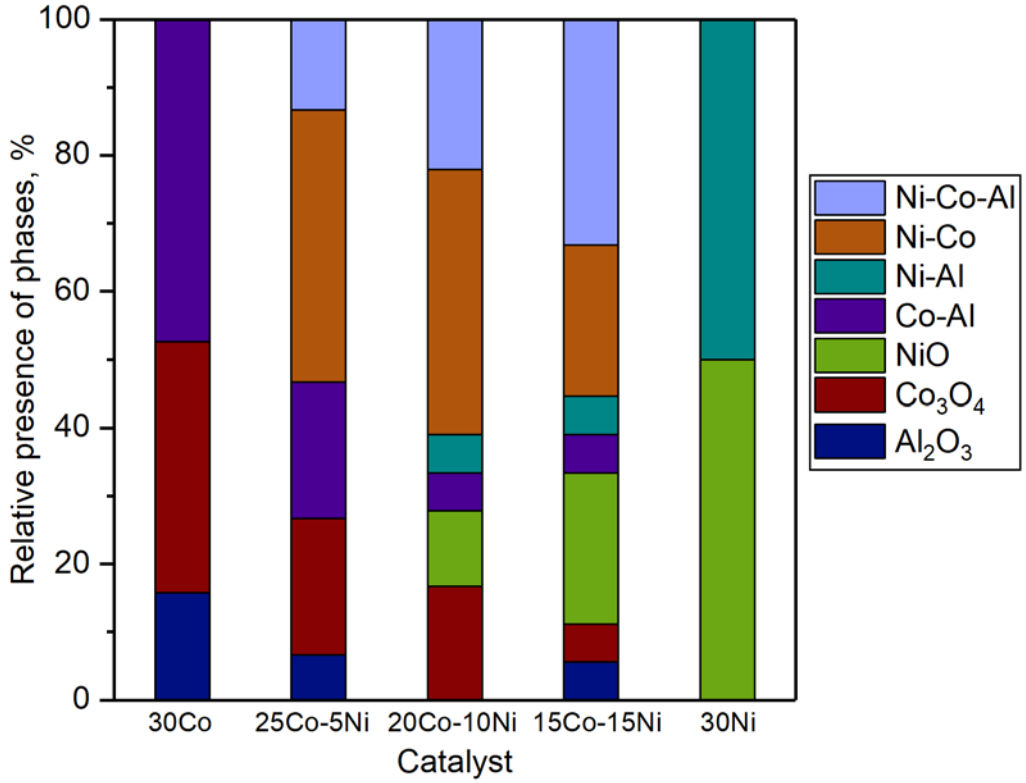
Relative presence of phases, %
100
80
60
40
20
0
30Co
25Co-5Ni
20Co-10Ni
15Co-15Ni
30Ni
Catalyst
Ni-Co-Al
Ni-Co
Ni-Al
Co-Al
NiO
Co_3O_4
Al_2O_3

FIGURE 7

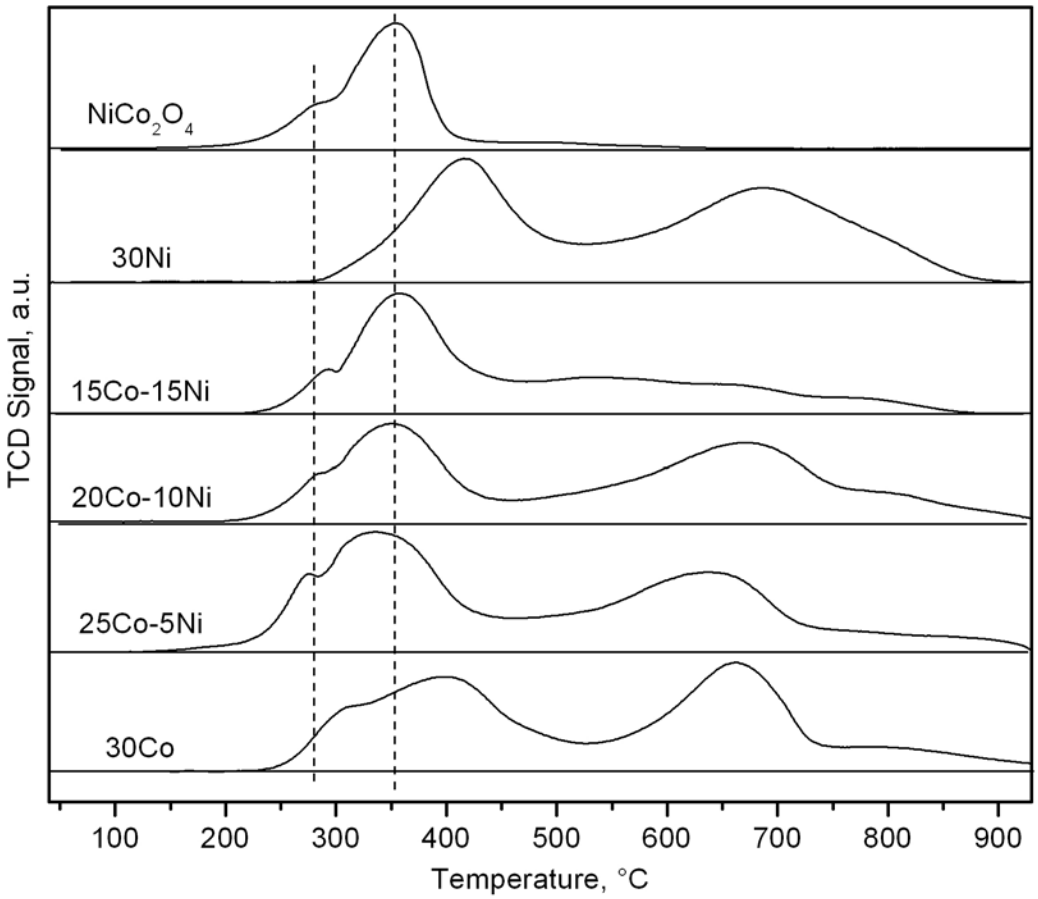
NiCo2O4
30Ni
15Co-15Ni
20Co-10Ni
25Co-5Ni
30Co
TCD Signal, a.u.
100
200
300
400
500
600
700
800
900
Temperature, °C

FIGURE 8

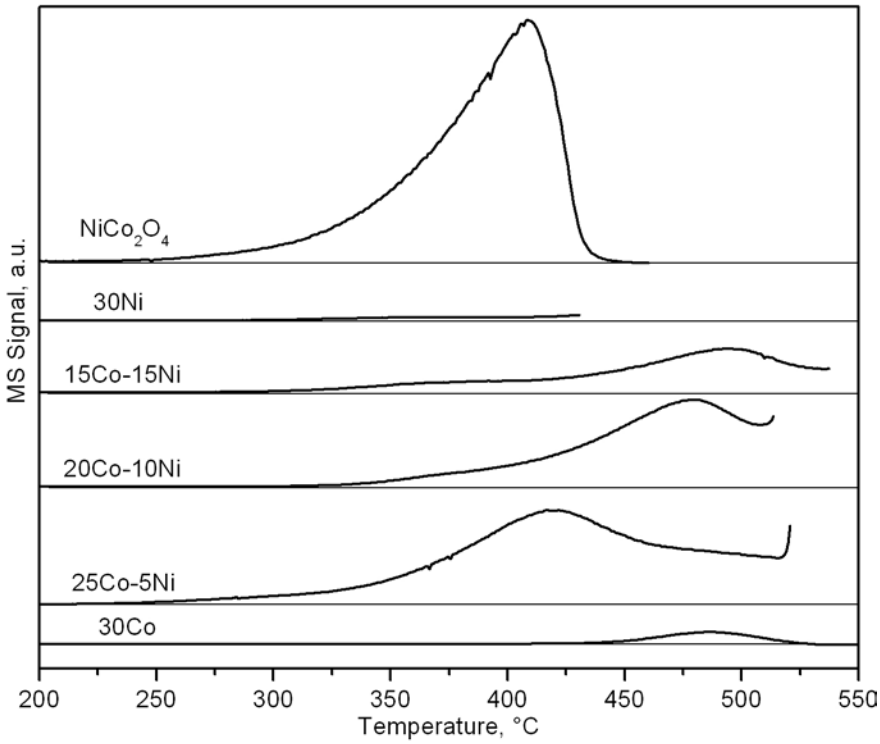
NiCo2O4
30Ni
15Co-15Ni
20Co-10Ni
25Co-5Ni
30Co
MS Signal, a.u.
200
250
300
350
400
450
500
550
Temperature, °C

FIGURE 9

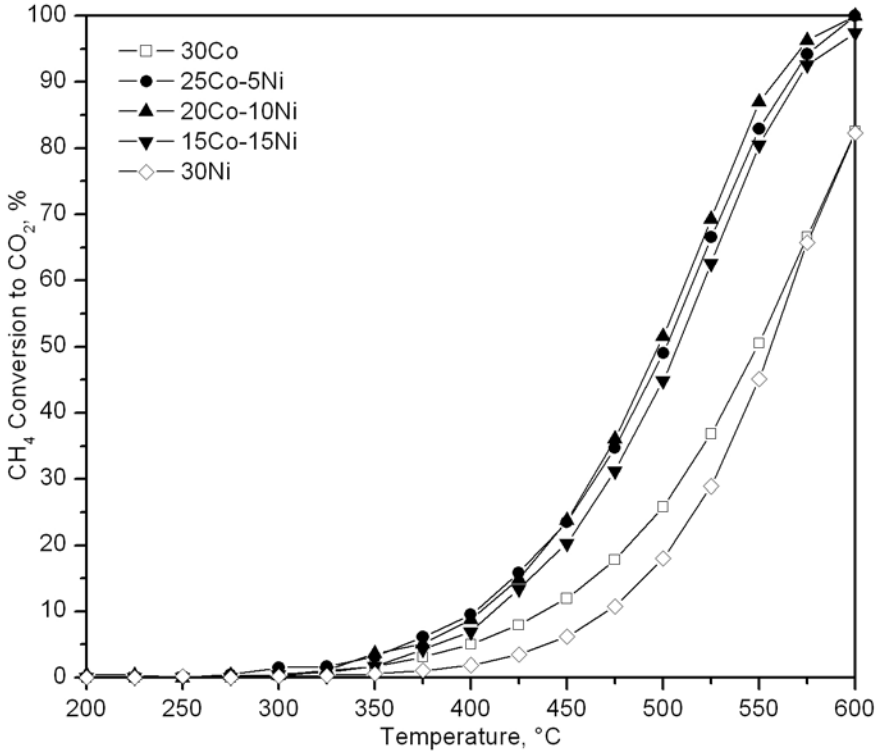
30Co
25Co-5Ni
20Co-10Ni
15Co-15Ni
30Ni
CH4 Conversion to CO2, %
Temperature, °C
0
10
20
30
40
50
60
70
80
90
100
200
250
300
350
400
450
500
550
600

FIGURE 10

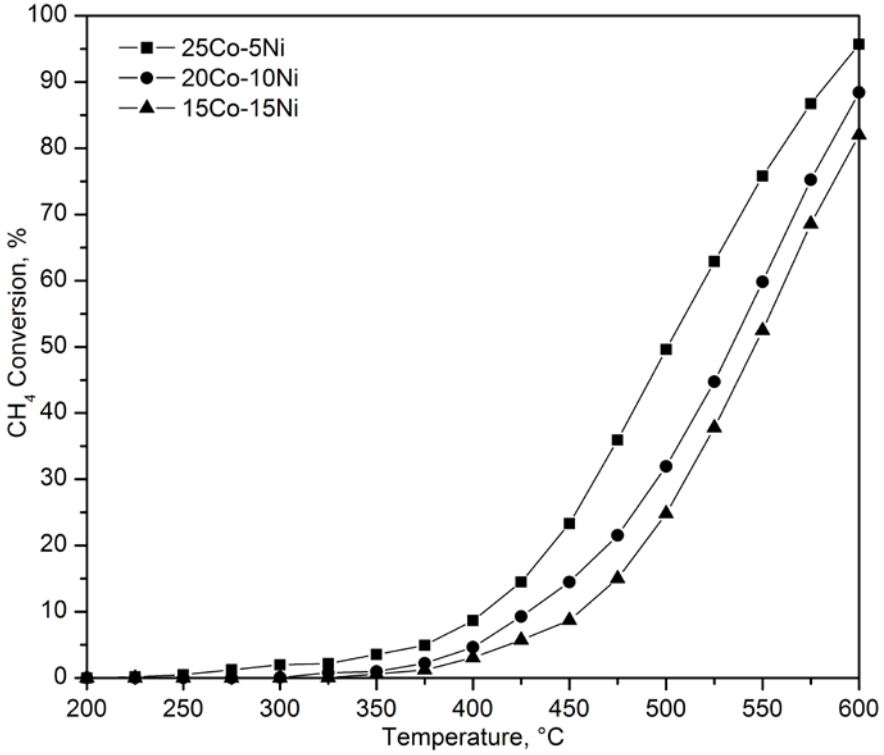
25Co-5Ni
20Co-10Ni
15Co-15Ni
CH4 Conversion, %
Temperature, °C
0
10
20
30
40
50
60
70
80
90
100
200
250
300
350
400
450
500
550
600

FIGURE 11

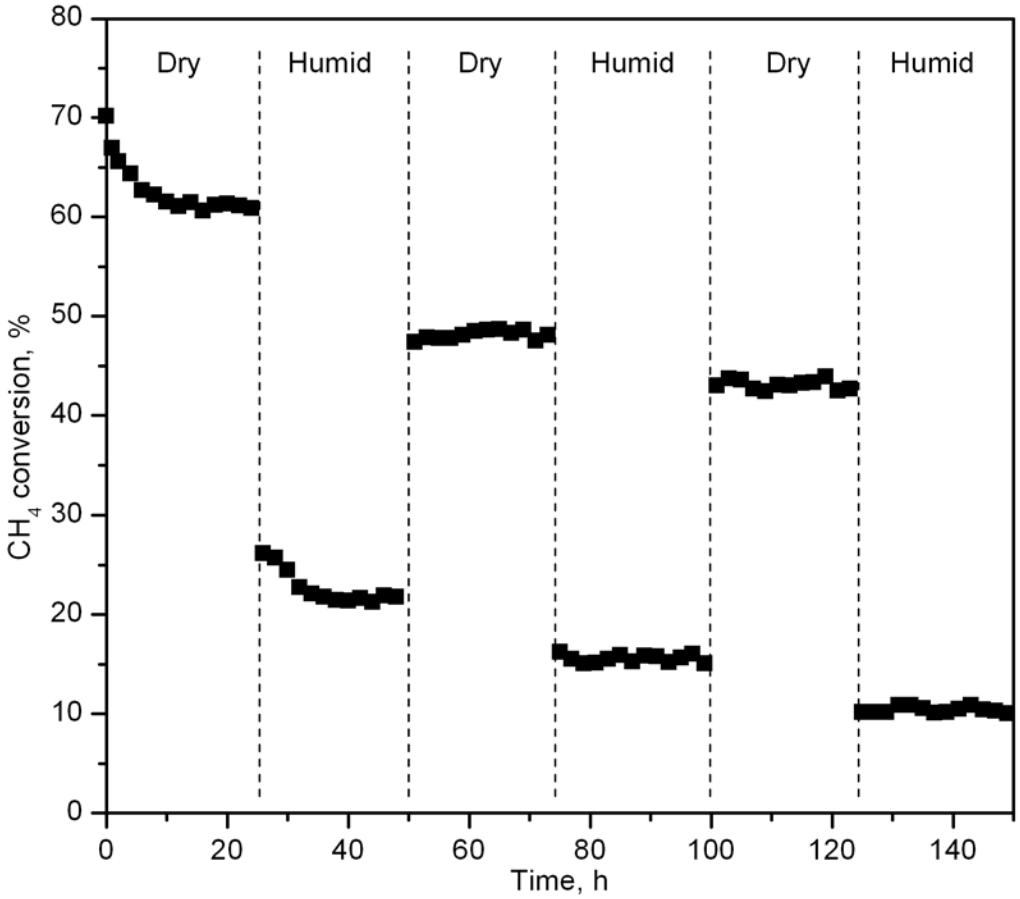
Dry
Humid
Dry
Humid
Dry
Humid
CH_4 conversion, %
Time, h
0
10
20
30
40
50
60
70
80
0
20
40
60
80
100
120
140

FIGURE 12